Atmos. Chem. Phys. Discuss., https://doi.org/10.5194/acp-2019-179
Manuscript under review for journal Atmos. Chem. Phys.
Discussion started: 13 March 2019

Atmospheric Chemistry and Physics Discussions

Observations and hypotheses related to low to middle free tropospheric aerosol, water vapor and altocumulus cloud layers within convective weather regimes: A SEAC^{4}RS case study

Jeffrey S. Reid[1]*, Derek J. Posselt[2], Kathleen Kaku[3], Robert A. Holz[4], Gao Chen[5], Edwin W. Eloranta[4], Ralph E. Kuehn[4], Sarah Woods[6], Jianglong Zhang[7], Bruce Anderson[5], T. Paul Bui[8], Glenn S. Diskin[5], Patrick Minnis[5], Michael J. Newchurch[9], Simone Tanelli[2], Charles R. Trepte[5], K. Lee Thornhill[5], Luke D. Ziemba[5]

[1]US Naval Research Laboratory, Marine Meteorology Division Monterey CA
[2]Jet Propulsion Laboratory, Pasadena CA
[3]General Dynamics, Naval Research Laboratory, Monterey CA
[4]Space Sciences Engineering Center, University of Wisconsin, Madison WI
[5]NASA Langley Research Center, Science Directorate, Hampton VA
[6]SPEC Inc. Boulder CO.
[7]University of North Dakota, Grand Forks, ND
[8]NASA Ames Research Center, Mountain View, CA
[9]Atmospheric Science Department, University of Alabama in Huntsville, Huntsville, AL

Key points:

1) Highly sensitive lidar and aircraft observations reveal thin aerosol detrainment layers from convection and their associated altocumulus clouds.
2) At 0^{o}C there is a proclivity for aerosol and water vapor detrainment from storms, in association with melting level Altocumulus shelves.
3) Detraining particles undergo chemical and microphysical transformations with enhanced nucleation in cleaner environments.

*Corresponding author: Jeffrey S. Reid (jeffrey.reid@nrlmry.navy.mil)

Atmos. Chem. Phys. Discuss., https://doi.org/10.5194/acp-2019-179
Manuscript under review for journal Atmos. Chem. Phys.
Discussion started: 13 March 2019

Atmospheric Chemistry and Physics Discussions

Abstract: The NASA *Studies of Emissions & Atmospheric Composition, Clouds & Climate Coupling by Regional Surveys* (SEAC^{4}RS) project included goals related to aerosol particle lifecycle in convective regimes. Using the University of Wisconsin High Spectral Resolution Lidar system at Huntsville, Alabama USA and the NASA DC-8 research aircraft, we investigate the altitude dependence of aerosol, water vapor and Altocumulus (Ac) properties in the free troposphere from a canonical August 12, 2013 convective storm case as a segue to a presentation of a mission wide analysis. It stands to reason that any moisture detrainment from convection must have an associated aerosol layer. Modes of covariability between aerosol, water vapor and Ac are examined relative to the boundary layer entrainment zone, 0^{o}C level, and anvil, a region known to contain Ac clouds and a complex aerosol layering structure (Reid et al., 2017). Multiple aerosol layers in regions warmer than 0^{o}C were observed within the PBL entrainment zone. At 0^{o}C there is a proclivity for aerosol and water vapor detrainment from storms, in association with melting level Ac shelves. Finally, at temperatures colder than 0^{o}C, weak aerosol layers were identified above Cumulus congestus tops (~0^{o}C and ~-20^{o}C). Stronger aerosol signals return in association with anvil outflow. In situ data suggest that detraining particles undergo aqueous phase or heterogeneous chemical or microphysical transformations, while at the same time larger particles are being scavenged at higher altitudes leading to enhanced nucleation. We conclude by discussing hypotheses regarding links to aerosol emissions and potential indirect effects on Ac clouds.

Plain language summary: In studies of the vertical transport of air pollution by clouds as well as pollution's subsequent impact on those clouds the scientific community often focuses on clouds with bases at the planetary boundary layer (such as typical fair weather cumulus) and the outflow from thunderstorms at their tops. However, new highly sensitive lidar systems demonstrate complex aerosol features in the middle free troposphere. Aerosol layers formed in convective outflow are explored and are shown to have strong relationships to mid-level tropospheric clouds, an important but difficult-to-model or monitor cloud regime for climate studies.

Atmos. Chem. Phys. Discuss., https://doi.org/10.5194/acp-2019-179
Manuscript under review for journal Atmos. Chem. Phys.
Discussion started: 13 March 2019

1.0 Introduction

Much of the focus of aerosol-cloud radiation studies (i.e., the first indirect effect) has been on either Planetary Boundary Layer (PBL) Stratocumulus (Sc) or Cumulus clouds (Cu, e.g., Twomey et al., 1977 and many subsequent citations), or the injection of aerosol particles and their precursors into the upper troposphere/lower stratosphere by deep precipitating convection (Cb, e.g., Pueschel et al., 1997; Kulmala et al., 2004; Waddicor et al., 2012; Saleeby et al., 2016), pyro-convection (e.g., Fromm et al., 2008; 2010; Lindsay and Fromm 2008) and volcanic activity (e.g., Jensen and Toon 1992; DeMott et al., 1997; Amman et al., 2003). However, there is a third important but often overlooked aerosol-cloud system related to mid-level clouds. Altocumulus (Ac) clouds in the lower to middle free troposphere (LMFT) are generated by numerous mechanisms (e.g., synoptic forcing, gravity waves, orographic waves), but are particularly prevalent in convective regimes (Heymsfield et al., 1993; Parungo et al., 1994; Sassen and Wang, 2012). Indeed, the above authors and others (e.g., Gedzelman, 1988) note these cloud types receive comparatively little attention in the scientific community relative to their importance. Forecasters sometimes ignominiously note the presence of Ac in convective environments as “midlevel convective debris.” Yet, Cloud-Aerosol-Lidar with Orthogonal Polarization (CALIOP) and CloudSat retrievals attribute to Ac as much as 30% area coverage in Southeast Asia and the summertime eastern continental United States (e.g., Zhang et al., 2010; Sassen and Wang, 2012; Zhang et al., 2014). This is in agreement with observer-based cloud climatologies (e.g., Warren et al., 1986; Warren et al., 1986).

A long-standing hypothesis by Parungo et al., (1994) suggested that globally increasing aerosol emissions would lead to higher mid troposphere aerosol loadings, in turn enhancing Ac reflectance and perhaps Ac lifetime. This is plausible, as Kaufman and Fraser (1997) mistook Sc and Ac clouds for Cumulus mediocris (Cu) in their analysis of cloud reflectivity and lifetime impacts by biomass burning particles (Reid et al., 1999). Lidar studies by Schmidt et al., (2015) showed significant sensitivity of cloud droplet size distributions to aerosol particles near cloud base. Yet Ac’s diurnal cycle, covariance with other cloud types including cirrus during convective detrainment, and sometimes tenuous cloud optical depth make Ac clouds difficult to characterize and monitor. In an inter-comparison study for Southeast Asia, Reid et al., (2013) found more diversity in midlevel cloud fractions between satellite products than at any other

87 level. Likewise, large scale models tend to underestimate Ac formation and liquid water content
88 (Barrett et al., 2017).

89 Ac cloud are prevalent in many forms such as: castellanus, an indicator of midlevel instability;
90 mountain wave lenticularis; and translucidus (or colloquially mackerel sky). One class of Ac
91 clouds is colloquially referred to as shelf clouds, caused in part by detrainment at mid-level from
92 deep convection (Fig. 1(a); see Johnson et al., 1999; Yasunga et al., 2006). These are not
93 assigned their own genus in the International Cloud Atlas (Cohen et al., 2017), but the generic Ac
94 is recognized as associated with the spreading of convective elements at a stable layer.

95 Ac shelves often form at 0^{o}C from deep convection or in association with mid-level inversions
96 (e.g., Johnson et al., 1996, 1999; Riihimaki et al., 2012). A primary production mechanism is
97 thought to be related to the formation of 0^{o}C stable layers initiated by the melting of falling
98 frozen hydrometeors and enhanced condensation to compensate for the cooling (Posselt et al.,
99 2008; Yasunga et al., 2008). Hydrometeor evaporation processes discussed in Posselt et al (2008)
100 have likewise been hypothesized to help form the inversion. This results in a thin cloud feature
101 forming just below the inversion. Shelf-like Ac from towering cumulus (TCu) are also frequently
102 observed (Fig. 1(b)), and may be related to the detrainment of overshooting tops around regional
103 0^{o}C stable layers formed by surrounding convection (Johnson et al., 1996), or upper level
104 subsidence. Combined Ac and associated Alto stratus (As) coverage can be high in convectively
105 active regions (Fig. 1(c)). Ac can also form overnight from the residual PBL in convective
106 environments and then burn off during the day (Fig. 1(d); Reid et al., 2017) or during fair
107 weather conditions just ahead of more active weather (Figure 1(e)). Ac by mesoscale lifting is
108 also common. Although sometimes geometrically thin with low liquid water contents, Ac can
109 generate copious virga (Figure 1(f)).

110 Compared to other cloud species, the relationship between LMFT aerosol layers and Ac clouds
111 has a small literature base. The largest fraction of papers relate to lidar observations of smoke
112 and dust as ice nuclei (IN) in mixed-phased alto clouds (e.g., Hogan et al., 2003; Sassen et al.,
113 2003; Wang et al., 2004; Sassen and Khvorostyanov, 2008; Ansmann et al., 2009; Wang et al.,
114 2015). However, cloud condensation nuclei (CCN) budgets for these cloud types have not been
115 studied in detail with in situ observations, particularly for entirely liquid clouds. The complex
116 mixed-phase nature of alto-level clouds and stratiform precipitation coupled with their thin

117 nature and low updraft velocities (Schmidt et al., 2014) likely lead to sensitivity to even small
118 perturbation in CCN concentration (Reid et al., 1999; Schmidt et al., 2015; Wang et al., 2015).
119 Clouds can serve as aqueous phase reactors of gas and aerosol particle species, even hosting
120 nucleation events (Hegg et al., 1991), while evaporating droplets and precipitation leave residual
121 aerosol particles. Given that Ac clouds are observed to have a strong impact in shortwave solar
122 radiation (Sassen and Khvorostyanov, 2007), the hypotheses of Parungo et al., (1994) are worthy
123 of consideration despite initial skepticism (e.g., Norris 1999). Only now are the tools becoming
124 available to quantitatively investigate further.

125 Observing the aerosol-Ac environment is challenging. The scarcity of data for alto-level aerosol
126 layers in the convective regimes where Ac clouds often form, combined with the contextual or
127 sampling biases inherent for the in situ observations of such layers and sun-synchronous polar-
128 orbiting aerosol observations, obscure the true importance of LMTF aerosol layers in
129 atmospheric aerosol lifecycle and Ac cloud physics. An opportunity for study arose with the
130 summer 2013 NASA *Studies of Emissions & Atmospheric Composition, Clouds & Climate*
131 *Coupling by Regional Surveys* (SEAC^{4}RS; *Toon et al.,* 2016) field mission. For SEAC^{4}RS, the
132 NASA DC-8, NASA ER-2 and Spec Inc Lear-25 aircraft were deployed along with ground assets
133 including the University of Wisconsin Space Science and Engineering Center (SSEC) High
134 Spectral Resolution Lidar (UW-HSRL) to examined the aerosol and cloud environment of the
135 summertime eastern United States (Toon et al., 2017; Reid et al., 2017). These observations
136 allowed for comprehensive measurements of the structure and microphysical properties of local
137 convectively generated LMFT aerosol layers.

138 SEAC^{4}RS provided a valuable but complex dataset-especially in the vicinity of active
139 convection. To simplify the analysis, this paper provides a case study of the covariability
140 between aerosol layers and LMFT Ac clouds in convective environments using observations
141 collected on August 12, 2013. This day was chosen due to the isolated regional nature of the
142 convection that occurred, and availability of ground based lidar and airborne DC-8 sampling.
143 This analysis will provide context for further exploration of the SEAC^{4}RS datasets.

144 For this analysis we define Ac consistent with the WMO definition (Houze 1993; WMO
145 https://cloudatlas.wmo.int/clouds-definitions.html last accessed Mar 2018) of mid-altitude (2-7
146 km) clouds that are a) liquid or mixed phase, and b) decoupled from direct surface forcing. We

147 begin with a brief description of data sets used in the remainder of the paper (Section 2). We then
148 provide an overall narrative of the meteorological situation on August 12 (Section 3) followed by
149 an analysis of UW-HSRL (Section 4) and data collected from a nearby storm by the DC-8
150 (Section 5). In the paper's discussion (Section 6), we explore commonalities in the two datasets,
151 and further explore hypotheses of LMFT layer characteristics, their origins, and relationships to
152 Ac clouds to set the stage for subsequent papers. A final summary and conclusions are presented
153 in Section 7.

154 2.0 **Data and Methods**

155 The analysis presented here centers around the August 12th 2013 SEAC^{4}RS airborne research
156 flight based out of Ellington Field, Houston TX (Toon et al., 2016). The Ellington deployment
157 for the SEAC^{4}RS mission was conducted from August 12th -September 23rd with three research
158 aircraft (NASA DC-8, NASA ER2, SPEC Learjet 25), an extensive ground network including
159 AERONET sun photometers (Holben et al., 1998; Toon et al., 2016), and the deployment of the
160 UW-HSRL to Huntsville (Reid et al., 2017). Comprehensive descriptions of the field assets is
161 provided in this section's cited papers; here we provide a short summary of datasets used in this
162 analysis.

163 2.1 UW-HSRL Deployment to Huntsville

164 LMFT aerosol and cloud layers were monitored by a 532 nm UW-HSRL system, deployed by
165 the NASA Cloud-Aerosol Lidar and Infrared Pathfinder Satellite Observations (CALIPSO)
166 science team to enhance monitoring at the Regional Atmospheric Profiling Center for Discovery
167 (RAPCD) lidar facility at the UAH National Space Sciences Technology Center (NSSTC)
168 building (-34.725 ^{o} N; 86.645^{o} W), from June 18 to November 4, 2013. The RAPCD facility is
169 located on the western side of the city of Huntsville at an elevation of ~220 m. Including
170 building height, the lidar transmitter was situated at 230 m above mean sea level (MSL). Overall
171 the local terrain is flat, with the exception of a line of hills protruding an additional 200-350 m
172 and located 10-15 km to the east and southeast. The UW-HSRL was hardened for continuous
173 use, and collected contiguous aerosol backscatter and depolarization data every 1 minute at 30 m
174 vertical resolution. The only significant notable outages were from August 20th -22nd and
175 September 13th-17th. UW HSRL observations can be visualized and downloaded through the
176 SSEC HSRL web page (http://hsrl.ssec.wisc.edu/), last verified in February 2019).

The UW-HSRL was able to extract the aerosol backscatter profile to very high fidelity. Unlike more common elastic backscatter lidar measurements that must de-convolve a combined molecular and aerosol signal in an inversion, HSRL systems can separate a line broadened molecular backscatter signal from the total backscatter signal via a notch filter (Eloranta et al., 2005, 2014; Hair et al;, 2008). The difference is used to calculate aerosol backscatter. For this deployment the UW HSRL performed with a precision in aerosol backscatter of better than 10^{-7} $(m\ sr)^{-1}$ for a 1 minute average, and 10^{-8} $(m\ sr)^{-1}$ for 15 minute averages. In comparison, Rayleigh backscattering is $1x10^{-6}$ $(m\ sr)^{-1}$ at 4 km, and $5x10^{-7}$ $(m\ sr)^{-1}$ at 10 km. Thus at 15 min averaging, precision is likewise better than 1 to 5% of Rayleigh.

By calculating the slope of the returned molecular scattering, aerosol light extinction can be directly calculated. However, as described in Reid et al., (2017), there are several caveats. First, there must be significant enough signal to calculate the slope; in this instrument, extinction must be greater than 0.1 km^{-1}. Second, one must account for an "overlap correction" in the near field, accounting for the fact that the telescope is not fully in focus until a range of about 4.5 km from the system. The signal below the 4.5 km level appeared to vary in time, sometimes hourly, during the daytime. Consequently, for the altitude range we will study here, it is best to rely on aerosol backscatter. Noting that extinction is simply the aerosol backscatter times the lidar ratio (S_a), here we assume a lidar ratio of 55 sr^{-1} as a baseline (Reid et al., 2017). Expected deviations from this baseline are discussed in the Results and Discussion sections.

In addition to the lidar, several other deployments to the UAH site are used here. Most notably, UAH was a Southeast American Consortium for Intensive Ozonesonde Network Study (SEACIONS) release site (http://croc.gsfc.nasa.gov/seacions/, last accessed December 17, 2018). Forty sondes were released between August 6th and September 21th, 2013, at 18:00-19:00 Z/13:00-14:00 CDT to coincide with early afternoon boundary layer conditions, mid-flight airborne activity, and the NASA A-train overpass. For August 12, 2013, the release time was 13:42 CDT, and is used here for situational awareness and the mapping of cloud and aerosol layers to their temperatures.

2.2 The SEAC^{4}RS DC-8 Operations

The DC-8 conducted 24 flights with patterns that covered the Western United States through the Southeastern United States (SEUS) and into the Gulf of Mexico. Flight patterns often included

three primary relevant components. 1) A ~100 km curtain wall pattern with multiple flat flight levels from 5 km to the near surface to collect free troposphere, entrainment zone, cloud base and near surface samples; 2) saw toothed transits to monitor the lower troposphere for chemistry applications; and 3) spirals in the vicinity of developing deep convection. Flight restrictions in the vicinity of Huntsville prevented vertical profiles directly over the UW-HSRL. Nevertheless, the DC-8 had ample opportunity to sample the SEUS' LMFT environment, in particular for the case of August 12, 2013 examined here.

The DC-8 hosted its most comprehensive instrument suite ever to support the chemistry, convection, radiation, and upper troposphere/lower stratosphere (UTLS) science goals and customers. However, for the particular test case and application examined here, there are several caveats worth noting. While the ground-based UW HSRL can detect the fine aerosol structure in convective environments and in the vicinity of Ac clouds, generating in situ observations to correspond to this structure is difficult. At flight speeds of ~120-150 m s^{-1}, the DC-8 is only in a detrainment patch for a few seconds, causing difficulty in differentiating small-scale aerosol features. Further, the massive payload of the DC-8, although comprehensive, also leads to functional problems as instrument calibration, maintenance, or scanning cycles were not synchronized. Shattering effects of liquid cloud droplets and ice further disrupted the sampling of the very near cloud environment. Thus, one cannot retrieve full complement of all data for an entire profile or flight component, let alone for individual features that the DC-8 might observe for less than 10 seconds. While the DC-8 carried a lidar system of its own, stand-off distances from the aperture and cloud heterogeneity prevented its use in this particular analysis. Nevertheless, the DC-8 hosted a number of instruments that can provide a valuable view of the overall aerosol and cloud structure in the August 12th 2013 convective environment which can be coupled with the lidar observations. These key instruments are listed here.

1) State variables: Navigation was derived from DC-8 housekeeping variables. Pressure, temperature and winds were measured by the NASA Ames Meteorological Measurement System (MMS, Scott et al., 1990). Moisture related variables were derived from the NASA Langley Diode Laser Hygrometer (DLH, Podolske et al., 2003; Livingston et al., 2008).

2) Aerosol physical and optical properties: Baseline aerosol number, size, and optical properties were derived from the Langley Aerosol Research Group Experiment (https://airbornescience.nasa.gov/instrument/LARGE, Ziemba et al., 2013; Corr et al., 2016) instrument set, which included continuously sampling nephelometer, CN, and optical particle encounters. The LARGE package monitored aerosol particles from ultrafine CN to an inlet cut point of ~3.5 μm, and units reflect volumetric scaling to a standard temperature and pressure of 20°C and 1013 hPa. To prevent any possible cloud water or precipitation shattering effects on the aerosol instruments, CN, nephelometer, and LAS data was heavily cloud screened with data points removed for one second before the arrival and two seconds after the exit of any cloud with LWC>0.005 g m^{-3}.

3) Aerosol chemistry: Aerosol chemistry was evaluated using data from the CU aircraft HR-AMS (Canagaratna et al., 2007; Dunlea et al., 2009; http://cires1.colorado.edu/jimenez-group/wiki/index.php/FAQ_for_AMS_Data_Users last accessed Mar 2018) that reports the composition of submicron non-refractory particles. Reported O/C and OA/OC ratios from this instrument were derived using the updated calibration of Canagaratna et al (2015). Unlike single particle instruments, the AMS is fairly insensitive to inlet artifacts during cloud penetration. Data points that were flagged as being potentially impacted by such artifacts (by monitoring excess water and/or zinc in the aerosol mass spectrum) were removed prior to analysis.

4) Cloud properties: Cloud detection properties were derived from the SPEC microphysics package (e.g., Lawson 2011; Lawson et al., 2001; 2006; 2010), in particular the Fast Cloud Droplet Probe (FCDP) which provided the core cloud liquid water product and the 2D-2 for ice identification.

5) Gas chemistry: While the DC-8 carried comprehensive gas chemistry instrumentation, for this overview case study we rely on CO from the Differential Absorption CO measurement (DACOM, Sachse et al., 1987; McMillan et al., 2011).

2.3 Ancillary datasets:

In the analysis presented here multiple data sets were examined, but for brevity are not shown in detail here. Regional meteorology was diagnosed through a combination of NEXRAD radar (NOAA NWS, 1991), GOES-13 geostationary and MODIS satellite datasets and models. Baseline meteorology was provided by a Coupled Ocean Atmosphere Mesoscale Prediction

Atmos. Chem. Phys. Discuss., https://doi.org/10.5194/acp-2019-179
Manuscript under review for journal Atmos. Chem. Phys.
Discussion started: 13 March 2019

Atmospheric Chemistry and Physics Discussions

System (COAMPS®) analysis including NEXRAD precipitation and wind assimilation (Zhao et al., 2008; Lu et al., 2011). Operational MODIS aerosol (MOD/MYD04, Levy et al., 2013) and cloud (MOD/MYD 06, Platnick et al., 2003; 2016) were also used. Geostationary imagery was generated at Space Sciences and engineering center with cloud products generated by Minnis et al. (2008). Regional aerosol concentrations were taken from South Eastern Aerosol Research and Characterization (SEARCH, Edgerton et al., 2015) and Chemical Speciation Network (CSN), and Aerosol Robotic Network (AERONET, Holben et al., 1998) sun photometer data. Back trajectories were utilized from HYSPLIT (Stein et al., 2015).

3.0 Regional context for the August 12th case

Analysis of the August 12, 2013 case study is greatly aided by context provided by a regional weather analysis guided by satellite and lidar observations. A more detailed meteorological analysis is provided in Supplemental Appendix A. In short, on August 12, 2103 the SEUS was in a fair weather summertime convective regime, with copious small convection, congestus and isolated CBs. Images of the cloud field from MODIS and on-aircraft photography are provided in Fig. 2 (including MOD/MYD cloud top temperatures), along with the afternoon radiosonde sounding at UAH in Fig. 3 (release 18:40 GMT; 13:40 local CDT time), including (a) temperature and dewpoint; (b) water vapor mixing ratio; and (c) wind speed and direction. The diurnal pattern of convection is also provided in NEXRAD composite radar images taken throughout the day, which are provided in Appendix Fig. A.2.

By daybreak on August 12th, the convection of the previous day had largely subsided over Alabama (Figs. A.2(b) and (c)). Northern Alabama experienced developing Cu and Ac, with cirrus (Ci) intermixed to the north in the morning hours (e.g., Terra MODIS 16:00 UTC, Figs. 2(a) and (c)) in association with the stationary front. A large area of optically thin ~0°C clouds, presumably melting level Ac, extended southward from the more convectively active regions to the northwest. Cloud fractions outside of the cirrus domain ranged from 70-90%. Just before the Terra overpass, isolated convection was initiated throughout the region, including several cells north and east of the UAH site. By early afternoon (Aqua MODIS 19:14 UTC, Figs. 2(b) and A.2 (d) and (e)), isolated precipitating cells were widespread across the region. At the same time, cloud fractions diminished significantly, with a notable reduction in mid-level Ac (yellow colors). Low level cloud fractions diminished up to ~60%, but there were larger numbers of isolated and higher-topped TCu.

297 Using the DC-8 forward-looking cameras during its flight on August 12, ~21:16 UTC, allows us
298 to categorize the cloud types and heights of the cloud bases and cloud tops of the observed
299 clouds at the time of the flight (Fig 2e-h). Forward camera images of the environment very near
300 the deepest convection are provided in Fig. 2(f), and (g), respectively, with a final nadir image of
301 the Ac field departing the Cb in Fig 2(h). TCu and Cbs were more isolated, relative to the Ac,
302 forming in association with the remnant outflow boundaries from previous storms, rather than in
303 organized and sustained lines. Clearly visible in Fig 2(e) is a cloud base delineating the mixed
304 layer and the PBL entrainment zone at ~1.5 km, corresponding well to the UAH sounding. This
305 entrainment zone was populated by Cumulus humilis (CuHu) to Cu with tops based on the DC-8
306 DIAL HSRL in the 1.5-3.8 km AGL range, functionally defining the top of the PBL. Larger Cu
307 occasionally rose to as high as 4-4.5 km, or to roughly the 0^{o}C level from the sounding. TCu rose
308 to 6-6.5 km, with isolated Cb tops at 12 km. Between the PBL top and the Cb anvils, layers of Ac
309 clouds were prevalent. Some of these Ac clouds are related to mid-level detrainment from Cbs,
310 others are clearly emanating near the tops of TCu (e.g., Fig 2(f)-(h)). Near surface haze was also
311 visible, with Aqua MODIS and AERONET reporting 550 nm AOD on the order of 0.25-0.35.
312 Reported $PM_{2.5}$ was on the order of ~8 μg m^{-3}.

313 At the time of the early afternoon UAH radiosonde release, the sounding was typical for the area
314 for a moderately unstable convective meteorological regime (Fig. 3), with the mixed layer and
315 top inversion at 1500 m MSL (1280 AGL; Fig. 3(a)). Water vapor mixing ratio (Fig. 3(b)) was
316 constant, as expected in the mixed layer, falling off rapidly with altitude above, and with small
317 perturbations associated with temperature inversions. Winds were near constant at 250^{o} above
318 the mixed layer, and with steady increases to 12 m s^{-1} at the 0^{o}C melting level at 4.6 km
319 providing only a modest amount of shear (Fig 3(c)). Derived CAPE from the UAH sounding was
320 1650 J kg^{-1} (moderate instability) consistent with TCu to isolated Cb development. As discussed
321 n the next section, the corresponding HSRL aerosol backscatter profiles for this release are in Fig
322 3(d)).

323 4.0 **Results I: HSRL observations**

324 While the above analysis qualitatively describes the nature of the cloud fields, the time series of
325 aerosol backscatter and depolarization from the UW-HSRL from August 12th, 0:00 UTC through
326 Aug 13, 09:00 UTC (Fig. 4 (a) and (b), respectively) provides a quantitative representation of the

intricate regional aerosol and cloud environment. Lidar data in Fig. 4 was averaged over 1 minute intervals and over 30 m vertical layers, and represents a time period that extended from local sunset of August 11th through daybreak on August 13th. Included for reference are ceilometer-like cloud bases identified in the lidar data for liquid and ice clouds (Fig 4(c)), with associated geostationary derived cloud tops. Recall, key temperature, water vapor and wind levels included from the August 12th, 18:40 UTC SEACIONS radiosonde release are further provided in Fig. 3(a), (b) and (c) respectively and HSRL aerosol backscatter profiles within +/- 3-hours in (d). Temperature levels from this release are included in Fig. 4. Likewise, mean and individual aerosol backscatter profiles (every other 5 minutes average, 30 m resolution) are included in Figure 3(d) for the two hours after the sounding when the DC-8 was sampling northern Alabama.

The meteorology and aerosol profiles depicted in Fig. 4 show considerable fine scale structure in cloud and aerosol features. Considered in concert with Fig. 3, Fig. 4 indicates this day is consistent with the description of the convective environment in Reid et al., (2017) for a similar August 8th 2013 case. Thus the description of the overall nature of the aerosol environment does not need to be repeated here in detail, other than to identify the key layers. During the two hour period surrounding the 18:40 UTC radiosonde release, there is: 1) A mixed layer that extends from the surface to 1500 m AGL, identifiable by constant ω_v (Fig. 3b) and an increase in aerosol backscatter in height due to increases in RH with height and hence hygroscopic growth (Fig. 3(d) and 4(a)); 2) Above the mixed layer inversion lies the entrainment zone, including visible detrainment layers; 3) As discussed above and shown in Fig. 2(e), the top of the PBL is ambiguous as it relates to cloud tops in a heterogeneous cloud field, but a clear reduction in aerosol backscatter is visible at 4 km, likely related to the tops of regional Cu; 4) A second drop in aerosol backscatter occurs at the 0°C melting level with on this day, 5) a final aerosol layer between 6-7 km which, as we discuss later, may be associated with cloud top detrainment from TCu. Assuming a baseline S_a= 55 sr^{-1} as derived by Reid et al., (2017) an aerosol backscatter of $1x10^{-6}$ $(m\ sr)^{-1}$ (yellow) is equivalent to an aerosol extinction of 0.055 km^{-1}. Integration of aerosol backscatter from the surface to 10 km for cloud free periods with this lidar ratio suggests a 532 nm AOD of ~0.17, dropping to 0.12 later in the day, identical to AERONET.

356 Moving from the sonde release to the whole period shown in Fig 4, the above description of the
357 thermodynamic and aerosol state of the atmosphere holds for the day. Clouds and precipitation
358 are clearly visible in the aerosol backscatter color scales as dark red (backscatter $>10^{-4}$ (m sr)$^{-1}$.
359 Comparing aerosol backscatter with depolarization for the whole column (Fig. 4(a) and 4(b)),
360 clouds dominated by ice are easily identifiable from liquid by depolarization values above 40%
361 (Sassen, 1991), although as discussed later in association with DC-8 observations, low
362 depolarization does not exclude the presence of ice. Large liquid water drops can also depolarize
363 the lidar signal and signify heavy precipitation, and are thus annotated on Fig. 4(a). Yellow
364 highlight boxes of interesting cloud and aerosol phenomenon are marked on Fig. 4(a), with
365 corresponding enhancements of key features in Fig. 5 derived from 10 second, 7.5 m data.
366 Finally certain cloud types are annotated including Ac, Sc, and Ci.

367 Expanding the analysis to include the early evening of the previous day, radar and satellite data
368 (Fig A.1 and A.2) indicated multiple Cbs at various states of lifecycle were within 15-30 km of
369 the UAH lidar site. Consequently, cirrus (notable by their high depolarization) was detected
370 through Aug 12, 2013 7:00 UTC (2:00 CDT) with "bases" for virga or ice falls between 8 to 13
371 km, or -35 to -57°C. Given that homogenous ice nucleation can begin at -37°C, except in the
372 most extreme conditions, at these temperatures water tends to be ice (Pruppacher and Klett,
373 1997; Campbell et al., 2015). Virga is observed at cloud bases at ~4.5 and ~8.5 km MSL,
374 highlighted in Fig. 5(a). Using depolarization, we can see the upper cloud at 8.5 km and -25°C
375 has ice virga emanating from super-cooled liquid water in classic Ac fashion. The cloud base at
376 4.5 km and 0°C is entirely liquid by lidar observation, although we expect mixed phase processes
377 at work above where the lidar beam was attenuated. This behavior in combination with local
378 NEXRAD radar data suggests this lower cloud feature is stratiform precipitation from the anvil
379 of a decaying system.

380 In the morning of August 12 until just after daybreak (sunrise ~13:05Z; 6:05 CDT), a strong
381 aerosol return was visible centered on the 1-1.5 km MSL/0.8-1.3 km AGL range, likely a residual
382 layer from the previous days PBL mixed layer (ML, to 1.2 km), or entrainment zone (EZ, ~2.5
383 km). This residual layer may have been transported from the east, but also may be a result of
384 nighttime cooling and enhanced relative humidity and particle hygroscopicity. Morning
385 Stratocumulus are embedded in this layer and small liquid water Ac cloud returns are also visible

386 in the morning (inset box Fig. 5 (b)), at 5:00 UTC at ~6 km (-7°C), 10:00 UTC 4 km (5°C), with
387 the strongest returns at the 4.7 km 0°C melting level at 12:00 UTC. These clouds likely originate
388 from convective detrainment of water vapor, such as from melting level detrainment of
389 convection (e.g., Fig. 1(a) & (b)) or from the tops of TCu clouds, sustained by cloud cooling.
390 Associated with these clouds are clearly visible individual pockets of aerosol particles on the
391 order of a few hundred meters high and 15-30 minutes in duration. With backscatter returns on
392 the order of 1 to $5x10^{-7}$ $(m\ sr)^{-1}$, such features are <5% of Rayleigh backscatter and demonstrate
393 the Ac are embedded in larger aerosol features. At wind speeds of 5-10ms^{-1}, these pockets are
394 between ~5-20 km wide.

395 In the early morning hours local time, tenuous clouds are also observed at 1 km within the ML
396 residual layer, likely nighttime radiatively driven Sc. By local daybreak, CuHu begin to more
397 systematically form at ~1 km due to solar heating at the surface, with cloud base heights
398 increasing to 1.5 km as the ML and PBL develop throughout the morning to early afternoon LST
399 (inset Fig. 5 (c)). Clouds also formed at daybreak at 1.5 km inside a PBL residual aerosol layer.
400 At this height, above the CuHu, these clouds are decoupled from surface forcing and are
401 optically thin suggesting they are Ac, even though they share their initial formation physics with
402 Sc earlier in the day. More interestingly, a second Ac deck formed shortly thereafter, with 2-2.5
403 km MSL bases that increased in height with time through the morning to a maximum height of
404 3.7 km (5.5°C), collinear with the depth of the mixed layer. These are highlighted in inset box
405 Fig. 5(c). Based on geostationary imagery, and as demonstrated in the comparison of Figure 2(a)
406 to (b), these clouds evaporated at noon local time, presumably under solar radiation. This
407 situation is similar to the case of Fig. 1(f). Interestingly, aerosol layers between the PBL clouds
408 and the Ac are also visible forming late morning at ~15:30 UTC, and increasing with height with
409 the developing PBL and the Ac clouds above. Cirrus also begins to advect over the site by
410 afternoon, largely detraining from thunderstorms to the north and west (Fig. A2 (b)).

411 By 23:00 UTC, a mature phase Cb spawned by the outflow of the storm sampled by the NASA
412 DC-8 4-5 hours earlier arrived at Huntsville, bringing showers to moderately heavy rain. The
413 remnants of the storm extend through the next day, producing Ac visible from August 13, 0:00
414 to 3:00 UTC between the 4.5 km melting level and 7 km (-12°C) and (Fig. 5(d)). These clouds,
415 most likely local in origin, are often categorized as convective debris Ac by the forecasting and

aviation community-an indicator of multi-level detrainment in the convective environment. An aerosol layer exists to approximately the 4.5 km 0°C melting level capped by Ac. Additional Ac exist above these embedded in faint but clearly visible aerosol layer features. Unlike the aerosol pockets earlier in the day, these features are much more limited in extent, no more than 200-300 m in depth.

As the PBL collapses during the evening, it leaves a 1 km AGL residual layer not unlike those present a day earlier. A final set of light showers from a decaying system occurs in after the early morning of August 13 at 7:30 UTC (Figure 5(e)). With another clear melting level visible in the depolarization data, this is likely residual stratiform precipitation like at the beginning of the timeseries. Similar to the beginning of the time series, ice precipitation from super-cooled liquid water clouds was also present.

5.0 Results II: DC-8 Observations of an August 12, 2013 storm outflow

The HSRL gives an excellent depiction of the overall aerosol backscatter and cloud phase over the course of the day, but it lacks the ability to provide microphysical and chemistry information on the aerosol particles themselves. For this purpose, we utilize measurements on the DC-8 that flew in the region on this day. The flight pattern on August 12th included a curtain wall over the Gulf of Mexico, saw tooth transit to a curtain wall over northeastern Alabama, and more saw tooth patterns to a spiral on the downwind side of deep convection developing over the northwestern corner of Alabama. This last maneuver in northern Alabama is marked on Fig. 2(b), and provided the day's only complete tropospheric profile. Being on the downwind side of the storm's trajectory, this profile also gives a snapshot of the aerosol environment detraining from an isolated storm being fed by a polluted boundary layer. As the storms later passed over Huntsville, observations collected by the DC-8 also provided context for the UW HSRL lidar observations described in Section 4. Fig. 2 includes forward and nadir images of the overall environment. However, the most representative depiction of the midday to early afternoon environment is provided in Fig. 2(e), taken at 10 km altitude just as the DC-8 started its return from sampling the storm. The region had a deck of CuHu and Cu with bases at 1.4 km MSL/~1.2 km AGL, delineating the PBL's mixed layer from its entrainment zone. As mentioned, the PBL top was more ambiguous, and is functionally defined by the tops of these clouds at ~2.5-4 km (e.g., Fig. 2(a)). TCu were observed, overshooting above the 0°C level, as were scattered Cbs

446 with tops at ~12-13 km. Ac were prevalent on the horizon, detraining both from overshooting
447 TCu and midlevel of Cbs.

448 Profile variables collected by probes on the DC-8 during the spiral initiated at 19:10:30 are
449 provided in Figure 6. Included are (a) temperature and dewpoint (of liquid water) and tracer
450 species (b) water vapor mixing ratio (ω_v) and CO. To depict particle scattering (c) provides the
451 DC-8 total ambient 550 nm light scattering and a parallel dry light scattering for fine particles
452 (<1 μm). For context also included on Figure 5(c) is the inferred light extinction derived from the
453 UW HSRL by assuming a lidar ratio of 55 sr^{-1}. The period of averaging for the HSRL data is
454 19:00-21:00 UTC, or essentially from the start of the profile until just before the storms passed
455 overhead. Total particle counts from the LAS and CN counters are plotted on Fig 5(d). To
456 prevent any possible cloud water or precipitation shattering effects on the aerosol instruments,
457 CN, nephelometer, and LAS data was heavily cloud screened with data points removed for one
458 second before the arrival and two seconds after the exit of any cloud with LWC>0.005 g m^{-3}.
459 Finally University of Colorado aerosol mass spectrometer organic material and sulfate is
460 provided in Fig. 5(e). Only under very heavy ice content conditions does AMS data need to be
461 expunged from the profile. To reduce noise, a 5 second boxcar average was applied to the
462 particle counter and AMS data. Also to improve readability of PBL features, similar plots from
463 0-4 km are likewise included as Figures 5(f)-(j) respectively.

464 The DC-8 profile depicts intricate layering behavior throughout the free troposphere in a fashion
465 consistent with the UW HSRL backscatter. As expected, the temperature profile is largely moist
466 adiabatic ~ 6° C km^{-1}, indicating an atmosphere that has been modified by convective processes.
467 Moist layers, well depicted in the dewpoint sounding when it converges with temperature, often
468 coincided with minor temperature inversions. For reference these layers associated with
469 dewpoint depressions <2 °C are labeled on Fig. 6 as lines, or for three deeper layers, shaded
470 bands. Characteristics of these layers are also provided in Table 1, and Appendix A.2 provides
471 images taken from the DC-8's forward video to provide visual context of the environment being
472 sampled. As expected, moist layers coincided with increases in ω_v. However these layers also
473 strongly coincided with increases in other tracer species such as CO and dry aerosol
474 concentration. In the following subsection, we provide a narrative starting with layers influenced
475 by PBL detrainment (PBL layers 1 and 2; Sec. 5.1) followed by upper free troposphere

detrainment by the Cb (UT layers 1-4; Sec. 5.2). Emphasis will then be placed on the nature of aerosol and Ac layers in the middle free troposphere (MT Layers 1-3; Sec. 5.3). Finally we will examine composition and particle properties between these layers (Sec. 5.4).

5.1 PBL Detrainment Layers

Our first area of examination is of detraining aerosol layers associated with the development of the PBL, with clouds ranging from CuHu to Cu and the occasional congestus. This baseline PBL environment is described in detail in Reid et al., (2017), and is the subject of a subsequent paper on particle transformation and inhomogeneity within the PBL. Here, we consider a few specific aspects of the DC-8 data set to aid in overall profile interpretation, and also in the analysis of covariability among aerosol, water vapor and Ac cloud formation in the middle troposphere.

To begin we examine the nature of the PBL's mixed layer as this is the "source" of the atmospheric constituents being convectively lofted. However, the observation of the PBL's mixed layer profile at the bottom of the profile is contrary to what one would expect. Most notably, the ω_v is not constant with height near the bottom of the profile, suggesting that either the environment is not well mixed or the DC-8 never made it into the mixed layer. Based on forward video (Fig A.3 (a)), the spiral was initiated below cloud base and there was a strong gradient in ω_v on approach to the spiral; in fact isolated showers were seen across the horizon. It is therefore likely that the mixed layer is influenced by regional gradients- a recurring problem with profiling with large and fast moving research aircraft. Likewise, at the start of the spiral, gradients are also detected in CO and aerosol variables. These gradients are good indicators of significant spatial variability of atmospheric constituents in the mixed layer. Using a single point at the top of the mixed layer just before ascent as a baseline (Table 1), ω_v and CO were at a maximum of the profile at 15.5 g kg^{-1} and 110 ppbv, respectably. CN was at 2300 cm^{-3}, and a LAS volume concentration of 2.8 μm^3 cm^{-3} for an index of refraction of polystyrene spheres, (n=1.55), consistent with AMS concentration of particulate organic matter and sulfate of 4.2 and 1.5 μg m^{-3}, respectively. The light scattering hygroscopicity of growth from 20-80% RH was 1.62, typical of the region (Wonaschuetz et al., 2012).

Within the nearest level to the surface (PBL Layer 1 in Fig. 6, ~1.6 km MSL, 1.4 km AGL) is a clear aerosol enhancement just at and above mixed layer top which we diagnosed at ~1.5 km through a combination water vapor and temperature and visual inspection of cloud base from the

506 forward video. An enhancement is expected in ambient scattering at the top of the mixed layer
507 due to the increases in humidity with height in the mixed layer coupled with aerosol
508 hygroscopicity. But just above the mixed layer there is an increase in CO, dry aerosol mass,
509 number, CN and scattering. This, like the mixed layer variables, might be an aliased signal, but
510 also is influenced by detrainment from the Cu clearly present (Figure A.3(b)). At Huntsville at
511 the same time as the DC-8 spiral, the unaliased HSRL profile showed classic increased aerosol
512 backscatter (and presumed extinction) to a maximum at a level of 2 km MSL, indicating the top
513 of the mixed layer and cloud base slightly higher than the spiral location. PBL layer 1 is made up
514 of consecutive spikes within ω_v, CO, dry light scattering, LAS and CN concentrations, and AMS
515 sulfate as the DC-8 passed through the top of the mixed layer and into the level of the lowest
516 cloud bases (~1.5km AGL; Fig. A.3 (b)). Dramatic increases in CN and sulfate in particular
517 suggest that this layer potentially hosted secondary particle mass production via detrainment
518 from nearby shallow clouds (e.g., Wonashuetz et al., 2012). Although RH values were on the
519 order of 85-90%, both the probe data and visual inspection of the video data show this peak is
520 not associated with any form of cloud contamination. Ultimately, evidence suggests that this
521 layer is detrainment of mixed layer air from small cumulus. Even though this location near the
522 Tennessee River hosts some sporadic industry on its shores, the nature of the tracers, such as
523 water vapor and CO, demonstrates this layer was convectively transported from above the mixed
524 layer by small Cu. Recent studies suggest that the oxidation of SO_2 to $SO_4^=$ in such clouds can be
525 extremely fast (e.g., Loughner et al., 2011; Eck et al, 2014; Wang et al., 2016).

526 The second layer analyzed, PBL layer 2, was much deeper than the first, at 2.5-3.2 MSL (Fig.
527 A.3 (c)). This layer can be classified as the upper portion of the PBL entrainment zone, where air
528 is actively mixing with the free troposphere above via detrainment from cumulus. The ω_v is
529 enhanced and, between clouds, relative humidity ranged from 80-90%. At times enhancements
530 existed in LAS particle number and in AMS sulfate and OC. Spikes in CN concentration reached
531 10,000 cm^{-3}, likely a product of convective boundary layer precursor emissions receiving high
532 actinic flux not only directly from the sun, but also reflected from nearby clouds (e.g., Radke and
533 Hobbs, 1991; Perry and Hobbs, 1994; Clarke et al., 1998). Also during the DC-8's transit of this
534 layer was a 15 second Cu penetration that included significant precipitation, although this period
535 is expunged from the aerosol particle counter record in Fig. 6. In the middle of this cloud, CO
536 reached 80 ppbv, indicating convective lofting of mixed layer air. It is this cloud that we believe

537 developed into the CB sampled. At the time of this first penetration, from visual inspection, the
538 cloud top could not have been more than ~1 km above the aircraft (Fig A.2 (c)), consistent with it
539 not being picked up with NEXRAD.

540 The PBL Layer 2 detrainment environment is discussed in detail in Reid et al. (2017), and owing
541 to convective pumping and cloud processing of mixed layer air and high relative humidity
542 contributes significantly to regional AOD variability. Sometimes described as cloud halo effects
543 to explain covariability in cloud fraction and AOD, this PBL Layer 2 is actually a wide spread
544 detrainment induced layer (Reid et al., 2017). This layer was visible not only on the DC-8
545 nephelometer and AMS data, but is also coincident with a strong aerosol return from the
546 Huntsville lidar, some ~100 km to the west. Notably, the top of this layer coincides with the
547 lifting aerosol layer topped by Ac clouds in UW-HSRL (Fig 1(f), Fig 3(a) and Fig 4(c)) and
548 serves as a potential boundary between the PBL and free troposphere.

549 5.2 Upper Free Troposphere
550 Moving from PBL influenced aerosol layers, we now briefly examine the region dominated by
551 convective outflow from the anvil, diagnosed as detrainment in association with ice. This altitude
552 domain is largely outside the scope of this paper, and will be discussed in detail in other
553 SEAC^{4}RS papers. Nevertheless, for completeness a brief description is provided here. Like the
554 top of the PBL, the bottom of the cirrus anvil outflow layer is ambiguous. From Fig. 4 and in
555 particular Fig 5(a), it is clear that liquid water could exist as high as 8.5 km, or ~ -21 ^{o}C,
556 although ice was clearly nucleating and falling below this liquid water. The first full ice layers
557 were experienced by the DC-8 at 8 km and 8.4 km (UT 1 and 2, Fig A.3 (g) and (h)) followed by
558 a second cirrus cloud (UT2) a third at 9.4 km (UT3; Fig A.3 (i)), and finally a deep cirrus
559 penetration from 10-11 km (UT4; Fig A.3(j)). Because cloud particles in these layers were
560 entirely made of ice, with ice water content approaching 1 g m^{-3}, aerosol size and scattering data
561 are not available; although prominent peaks in CO, sulfate, and particulate organic matter are
562 found at each level indicating convective pumping and detrainment. From an aerosol point of
563 view, it is obvious that significant enhancements in particle mass and number exist on either side
564 of the cirrus layer. Notably the boundaries of these layers were enriched in organics relative to
565 sulfates, and CN>10 nm concentrations were on the order of 10,000-20,000 cm^{-3}, particularly
566 above 9.5 km. Indeed, observations suggest that deep convection is highly efficient at
567 transporting boundary layer air through to the anvil (Yang et al., 2015).

Atmos. Chem. Phys. Discuss., https://doi.org/10.5194/acp-2019-179
Manuscript under review for journal Atmos. Chem. Phys.
Discussion started: 13 March 2019


Atmospheric Chemistry and Physics Discussions

568 5.3 Middle Free Tropospheric Layers
569 The focus of this paper is on the middle tropospheric detriment layers, bounded below by the
570 primary PBL detrainment layer and its associated Ac clouds and above by the anvil cirrus, both
571 described above. Within the middle troposphere there were numerous perturbations in water
572 vapor, CO, and aerosol features. In particular, three coincident water vapor, CO and aerosol
573 layers were observed in the DC-8 spiral, clearly associated with liquid water clouds (MT Layers
574 1, 2, and 3; Fig A.2 ((d), (e), (f)). Starting from the bottom of the free troposphere and working
575 upwards, a slight inversion at 4.1 km delineated a rather minor water vapor and aerosol layer
576 (Fig. 6 MT1; Fig. A.2 (d)), which, like Layer PBL2, spanned both the DC-8 profile and the UW-
577 HSRL lidar at Huntsville. The inversion associated with this layer was a 200 m deep area having
578 a near constant temperature of 3.4^{o}C. Visual inspection of video data suggests this level was
579 associated with the maximum heights of the larger Cu and likely represents the very top of
580 convective pumping by larger boundary-layer clouds (Fig. A.3(d)). Such an interpretation is also
581 consistent with this layer delineating a drop in aerosol light scattering and mass which has likely
582 detrained from these larger clouds. Yet coincident with this inversion is a small spike in particle
583 number, as measured by the CN counter. The similarity of this layer to PBL2 is noticeable, even
584 if ejections are more sporadic than the smaller and more numerous cumulus clouds in the region
585 that define PBL2. These layers may be isolated, or be associated with a more organized region,
586 but they nevertheless show the lofting of mixed layer air into the free troposphere. Indeed, this
587 layer reminds us that in convective environments the physical top of the PBL is difficult to
588 define; the boundary between the cloud tops and the free troposphere is variable.

589 Special attention is paid here to the next two layers (MT 2 and MT 3) where significant
590 perturbations to tracer and aerosol loadings were associated with thin Ac cloud decks. Within
591 MT2, a strong aerosol return was present at 4.6 km associated with a shelf cloud deck at ~0.5^{o}C
592 detraining from the sampled Cb (Fig. 2(d) and Fig. A.3 (e)). MT3 contained a deeper layer of
593 isolated Ac clouds from ~6 to 7 km (-6 to -12^{o}C; Fig. A.3(f))). Unlike layers below these, they
594 are not directly observed at Huntsville, but are similar to a case earlier in the day and after the
595 storm passes later in the day (e.g., Fig. 5(b) and (d)). Detailed timeseries of data as the DC-8
596 passed through these two layers are presented in Figure 7.

597 MT2 at 4.6 km was targeted for direct penetration by the DC-8 because it represented a classic
598 melting level Ac detrainment shelf commonly observed around the middle of Cbs (e.g., Fig. 1(a);

599 Johnson et al., 1996; Posselt et al., 2008). The DC-8 approached the cloud from the side at a
600 slow climb rate (~ 1 m s^{-1}), and flattened out for Ac cloud sampling, followed by a more
601 accelerated climb (Fig. 7(a)). Consequently, the DC-8 captured the environment below and to the
602 side of the Ac deck, and the Ac deck itself. Given the air speed of ~156 m s^{-1}, the 50 second
603 timeseries for this aerosol and cloud layer spans ~8 km. On approach, water vapor, CO, dry light
604 scattering and aerosol mass species also increased in a layer perhaps only 200 m thick. Water
605 vapor changed in a series of steps, suggesting coherent layers, including a very sharp drop in
606 water vapor for only a few seconds just before cloud penetration, only to drop again on exit. The
607 drop in ω_v and cloud liquid water was immediately below a 2°C magnitude temperature
608 inversion.

609 Aerosol particle counts for d_p>0.1μm (and particle volume, not shown) also increased on
610 approach to the Ac. Total CN (d_p>10 nm) however dropped precipitously suggesting an overall
611 shift in the background size distribution in an environment that disfavored nucleation. Cloud
612 penetration lasted ~20 seconds (~3 km) and cloud liquid water contents ranged from 0.12 to 0.18
613 g m^{-3}. Droplet effective radius from the cloud probes (not shown) was consistently in the 4.5-6
614 μm range. Not surprisingly with a cloud temperature of ~1°C no ice was present. While aerosol
615 number or size distributions are unavailable during cloud sampling due to inlet shattering, CO
616 clearly peaked within 200 m of the altitude of the cloud. Yet, the AMS showed a decrease not
617 only within the cloud, but also just before cloud entry. As the DC-8 climbed up and away from
618 the Ac deck, LAS particle counts and AMS OC and sulfate dropped, while CN returned to
619 baseline levels and even spiked for a short period. Overall, MT2 observations match qualitatively
620 what was seen in the HSRL data, with the cloud resting on the top of the aerosol layer.

621 While MT2 was associated with a thin detrainment shelf, Layer MT3 was representative of a
622 much deeper layer of convective detrainment, spanning the 6-7 km level. These layers can be
623 visualized in the Huntsville HSRL data in Fig. 5 (b) and (d). Sampling of this layer was in the
624 form of steps (Fig 7(g)). Throughout this layer, ω_v and relative humidity varied in such a way
625 that this overarching layer is most likely an agglomerate of many layers. The existence of several
626 thin layers at various heights may result from detrainment at the tops of terminal congestus with
627 termina at different levels (Moser and Lasher-Trapp, 2017). Consequently, very faint Ac clouds
628 were visible on the video (e.g., Fig. A.3. (f)), though there were few actually cloud penetrations.

629 The clouds sampled had very meager liquid water contents (<0.01 g m^{-3}); barely clouds. Yet,
630 these clouds were mixed phase with ice clearly visible in 2D probe data at temperatures of -10^{o}
631 C, (Figure A.4; annuluses are also ice out of focus). Such ice is not noticeable in lidar data, as
632 optics may be still dominated by spherical liquid droplets. Thus, this observations suggests that
633 low depolarization observations cannot exclude the presence of ice,

634 For most of MT3, ω_v and CO varied in concert. However, at the very top of the level, they
635 quickly become anti-correlated-suggesting water vapor at this location is not being brought from
636 the boundary layer. Instead, it may be from entrained air along the sides-perhaps along cloud
637 edges air entraining in is the first to detrain out (Yeo and Romps, 2013). Aerosol data is not
638 much more enlightening. Aerosol mass was rather steady, and at reduced concentration than its
639 lower level counterparts. At the same time, spikes in aerosol counter and nephelometer data
640 occurred near clouds, and may just as easily be a result of droplet shattering artifact rather than
641 convective pumping.

642 5.4 Vertical Profile Aerosol Chemistry and Mass
643
644 5.4.1 H_20 and CO
645 Previous subsections in Section 5 describe the nature of individual detrainment layers. In this
646 final subsection, we provide a closer examination of differences in their properties. If we
647 conceptualize the environment as being influenced by shallow to deep injections of mixed layer
648 air being convectively transported to the free troposphere by clouds entraining and detraining air
649 along the way, it is best to start with reliable tracers such as CO. Figure 8 includes profiles of the
650 ratio of aerosol number and mass to excess CO.

651 Paramount to all subsequent interpretation of the profile is the molar ratio of excess water vapor
652 to CO. Whereas we can take background CO value of 60 ppbv (or any nearby value as long as
653 we are consistent), water vapor is a bit more problematic. We derived excess water vapor by
654 taking advantage of the deep convection horizontal scope of several hundred kilometers upwind
655 of UAH. A background value was derived from the average mixed layer mixing ratio, followed
656 by a 4th order polynomial fit against pressure above (r^2=0.99) . The calculated excess $\omega_{\underline{v}}$ between
657 the DC-8 and UAH sounding is provided in Fig. 8(a). As expected, ω_v is enhanced in the vicinity
658 of convection, notably in the mixed layer, as well as individual PBL and mid-level detrainment

659 layers, such as 3 km (PBL2), 4.6 km (MT2, 0°C), 6-7 km (MT3). Water vapor is also more
660 broadly enhanced in the upper troposphere layers (UT1-4).

661 Moving from establishing the background water vapor profile, we next consider how a parcel of
662 air lofted into the PBL deviates from textbook descriptions during deep convection. If the parcel
663 ascends without mixing, the water vapor mixing ratio is expected to decrease with altitude, as
664 temperature decreases at the moist adiabatic lapse rate and water vapor is removed by
665 condensation and precipitation. In contrast, CO is expected to remain constant over the time
666 scale of convective ascent. In reality, the vertical profiles of both constituents are modified by
667 entrainment/detrainment processes, and theory and numerical experiments indicate there are few
668 truly undiluted parcels to be found anywhere in regions of shallow or deep convection (Zipser
669 2003; Romps, 2010; Romps and Kuang, 2010). Parcels that ascend in a region near the core of
670 convection (far from the cloud edge) may conserve CO and approximately follow a moist
671 adiabat. Parcels closer to the cloud top and edge will undergo mixing with air that has originated
672 from various levels inside and outside of the cloud, and may reflect multiple entrainment-
673 detrainment events (Yeo and Romps, 2013). The ratio of water vapor to CO concentration in
674 undiluted ascent should be uniquely determined by the parcel's initial properties in the mixed
675 layer, and departures from this ratio within the cloud reflect the action of mixing. Outside of the
676 cloud, the situation is a bit more complicated. We expect water vapor content to decrease with
677 height, and, if CO is well mixed, then the concentration will be constant with height. Increases in
678 the ratio of water vapor to CO with height reflect the action of detrainment from convection, as
679 water vapor decreases with height more rapidly than CO.

680 The 0°C melting level is further related to the the air parcel characteristics. The molar profile of
681 excess H_2O to CO ratio is provided in Figure 8(b), and throughout the lower troposphere the
682 ratio increased to a maximum at the 0°C melting level. This increase reflects a more rapid
683 decrease in CO with height relative to water vapor, and is punctuated by two local maxima in the
684 ratio at 1.5 km and 3 km above the surface. Above the melting level, the ratio of H_2O to CO
685 precipitously drops, then exhibits local maxima at 5 km and 5.5 km.

686 Examining possible causes of the water vapor and CO ratio variability in the vertical above the
687 0°C melting level entails a closer examination of the impacts of detrainment on an air parcel.
688 Detrainment of air from convection results in local increases in both water vapor and CO;

689 however, water vapor content in detrained air will be greater than CO due to evaporation of
690 cloud condensate. The general increase in water vapor to CO ratio indicates the repeated action
691 of entrainment/detrainment (and evaporation of cloud condensate) around developing cumulus
692 clouds, while local maxima in water vapor to CO ratio reflect the action of enhanced detrainment
693 at specific levels; in this case, the tops of CuHu and Cu at 1.5 and 3 km, respectively. Detraining
694 air from congestus and deep convection at the melting level provides the strongest local source
695 of water vapor (direct and via evaporated cloud), and also the largest water vapor to CO ratio.

696 Contrary to the spikes in water vapor content caused by detrainment, immediately above the
697 melting layer, water vapor content is very low as this air originates in the middle and upper free
698 troposphere (c.f., Figs. 4 and Posselt et al. 2008). CO contently remains relatively high, since CO
699 is relatively well mixed in the middle and upper free troposphere (Fig. 5b). The near
700 discontinuity in water vapor content in the vertical, coupled with relatively small changes in CO,
701 result in the rapid decrease in water vapor to CO ratio above the melting layer. Relatively high
702 CO concentrations in the air detrained at and below the melting layer can be seen in the profile of
703 CO (Fig. 5b) and in the aerosol number to CO ratio maxima in Fig. 7b. Above the melting layer,
704 such as in the 6-7 km region (MT #3) thin layers of high water vapor to CO ratio are likely due to
705 detrainment from cumulus congestus clouds.

706 **5.4.2 Aerosol Mass**

707 Moving to aerosol particle profiles, different aspects of convective transport reveal themselves.
708 The ratio of LAS particle concentration (d_p>0.1 μm, representing the accumulation mode) and
709 CN (d_p>10 nm, representing the nucleation mode) to CO is presented in Figure 8(c). Relative to
710 CO, accumulation mode particles largely drop continuously in number from the surface to 0°C
711 level. Positive perturbations exist within the PBL and MFT aerosol layers as diagnosed in Fig. 6.
712 At heights above the 0°C level, the accumulation mode to CO ratio stabilizes at lower
713 concentrations with occasional layers. There is some difference in light scattering (Fig. 8(d)) and
714 OC and sulfate from the AMS ((Fig. 8e)), where we find mass enhancement in the PBL
715 detrainment zone.

716 Nucleation mode aerosol becomes more prominent with height owing to more intense solar
717 radiation and a decrease in available accumulation mode surface area. Nucleation rates of

718 particles from precursors detrainment from anvils can be rapid (Waddicor et al., 2012).
719 Detrainment layers host strong positive and negative perturbations in CN count, which does not
720 project significantly onto light scattering or mass, inverse with the concentration of accumulation
721 mode particles which do project strongly onto optical observables.

722 To explore variability in particle size distributions in the vertical, Fig. 9(a) and (b) provides LAS
723 number and volume size distributions for key levels throughout the profile, and is consistent with
724 what can be inferred from Figure 8. Best fit baseline particle size distribution within the mixed
725 layer suggest Count Median Diameter (CMD) and Volume Median Diameter (VMD) of 0.14 and
726 0.25 μm, respectively. At the first layer (PBL 1), dry particle size CMD and VMD increases to
727 0.16 and 0.28 μm, respectively, at the same time of increases in particle mass relative to CO.
728 This is all consistent with secondary aerosol particle mass production on exiting particles. After
729 this point, we find a reversal in particle CMD and VMD with height. This is suggestive of
730 precipitation scavenging of larger particles in larger clouds the deeper the detrainment. That is,
731 particles that are detraining from smaller non-precipitating clouds keep their secondary produced
732 mass. However these same aerosol particles that enter deeper precipitating clouds not only lose
733 their larger particles due to droplet nucleation, but also the recently gained secondary mass.
734 Nevertheless, significant aerosol mass from the boundary layer still be ejected in the anvil as
735 evidence in the 9-11 km altitude range in Figs 8 (d) and (e).

736 **5.4.3 OC and Sulfate**

737 The 0^{o}C level is clearly a delineator in the sulfate to OC ratio (Fig. 8(f)). Near the surface the
738 ratio of sulfate to OC is ~0.4. In the first PBL detrainment layer (PBL1) there is a doubling of
739 sulfate relative to CO. Such a mass increase relative to CO may be indicative of secondary
740 aerosol production-and indeed sulfate peaks in this layer not only against CO, but also relative to
741 OC (Fig. 7(e, f)). Particulate organic matter mass relative to CO peaks in PBL Layer 2, but with a
742 reduction in sulfate. Detrainment from this layer is associated with deeper clouds, including
743 warm precipitating clouds in the immediate vicinity. Thus, sulfate particles may be preferentially
744 scavenged.

745 The ratio of sulfate to OC further changes systematically through the profile, decreasing to a
746 minimum just below 4 km. This, coupled with the decrease in accumulation mode number

relative to CO, may be a further indicator of aerosol particle processing and scavenging in clouds. Above 4 km, sulfate increases again, perhaps due to oxidation of residual interstitial or dissolved but on oxidized sulfur species in either Ac clouds or in gas phase. This increase may also be related to the relative mass distribution within detraining cloud droplets. Sulfate mass fractions do appear to recover in the upper troposphere, perhaps due to homogenous nucleation of the small amount of SO_2 detraining from sublimating ice.

6.0 Discussion-combining datasets and hypothesis development

The purpose of this paper is to demonstrate on a canonical day that aerosol layering characteristics in the free troposphere and PBL entrainment zone are delineated by cloud structure and its associated thermodynamic profile. Examination of this day leads to many questions about aerosol processes and potential impacts or feedbacks with understudied Ac clouds. In the following section we use the combined datasets from the UW HSRL and the DC-8 aircraft to formulate several hypotheses about Ac formation that need further attention by the community.

6.1 Hypothesis: Ac cloud's low liquid water and slow updraft velocities are susceptible to small changes in the CCN population:

One of the most remarkable aspects of next generation lidar systems such as the UW HSRL used here and new Raman systems such as described in Schmidt et al., (2015) is their ability to observe intricate aerosol features at very low particle concentrations. Fig. 3(d), 4 and 5 demonstrate fine coherent structure of aerosol layers in the free troposphere that, in the past, were rarely quantified. Even with aerosol backscatter levels at or even under $<5x10^{-8}$ $(m\ sr)^{-1}$, or <5% of Rayleigh backscatter, aerosol layers of only a 100 to a few 100 meters thickness are clearly visible, and can persist for hours undergoing gravity wave undulations along with gradual changes in observed layer height at the meso to synoptic scales. Ac are often associated with observed aerosol layers, and the clouds we observed had very low liquid water contents of a few tenths of a g m^{-3} at most (e.g., Fig. 7). Drawing from parallels to Stratocumulus (e.g., Martin et al., 1994; Platnick and Twomey 1994; Ackerman et al., 1995), or the very limited available measurements of such relationships for Ac in the field (e.g., Reid et al., 1999; Sassen and Wang, 2008; Schmidt et al., 2015), we would expect Ac cloud's low liquid water and slow updraft velocities to have significant sensitivity to CCN populations. It stands to reason that aerosol-Ac

777 sensitivities can then project onto cloud reflectivity, cloud lifetime and consequently the local
778 energy budget. Thus trends, in global aerosol populations, that regionally have strongly varying
779 signal and sign, (e.g. Alfaro-Contreras, et al., 2017) may very well result in large scale trends in
780 Ac cloud cover (e.g., hypotheses by Parungo et al., 1994) or reflectivity. However estimating
781 CCN concentration based on the regional aerosol loading is difficult. One is attempting to
782 estimate the properties of a very thin aerosol layer with high complex relationships to the
783 boundary layer and regional convection.

784 Given the difficulties in modeling aerosol entrainment and entrainment processes, one might
785 think that direct observation would be much more straightforward. But the convection-Ac
786 system is very difficult to monitor. Despite improvements to lidar systems, data from lidars are
787 underdetermined. Aerosol backscatter and/or extinction, even spectrally resolved, are only semi-
788 quantitatively related to CCN concentrations. To provide aerosol microphysics information, an
789 aircraft such as the DC-8 is required. But in the context of the aerosol structure highlighted in Fig
790 5, aircraft sampling is hopelessly aliased. This is compounded by the typical structure of a thin
791 Ac deck above its associated thin aerosol layer. Broad sampling of the free troposphere would
792 reveal only period collinear perturbations, and aircraft location relative to the rest of the fine
793 aerosol structures would remain unknown. Even if the DC-8 were directly over the Huntsville
794 site, interpretation of the data would be complicated by features such as gravity waves and halos
795 around individual clouds. Therefore, much effort is required on sampling methods to address this
796 hypothesis.

797 6.2 Hypothesis: CN events can sustain and enhance CCN populations in Ac clouds

798 The impact of aerosol dynamics of the region must be considered when addressing a number of
799 science questions. Aerosol backscatter is dominated by accumulation mode particles that, owing
800 to their size, also make the best CCN. While there are copious CN, there are few particles in
801 number of any appropriate size to behave as CCN (~100 cm^{-3} or less in the LAS at altitudes
802 above the $0^{o}C$ level). Considering the proclivity of CN nucleation events, and the overall
803 increasing numbers of CN at higher altitudes, the CCN versus optical detection relationship is
804 complex, (e.g. Schmidt et al., 2015). Enhancements in accumulation mode particles near Ac
805 appear to be anti-correlated with CN for this case-likely due to available surface area for
806 secondary mass production and or coagulation. At the same time, explosive nucleation events are

807 visible and expected. This all leads to questions about layer flow dynamics in and around Ac and
808 their associated aerosol layers and/or halos. Does the cycling of air through an Ac feedback into
809 its own CCN budget? Does non-precipitating cycling enhance particle size and hence CCN
810 number for any given supersaturation? In precipitating Ac, where are replacement CCN coming
811 from, and do nucleating CN ever offer a supply? Or, as a hypothesis, perhaps CN events can
812 sustain and enhance CCN populations in Ac clouds. The null hypothesis would then be that CN
813 are consumed in individual droplets and have little overall effect in clouds with such meager
814 updraft velocities and super saturations. This topic in particular needs to be addressed in highly
815 detailed modeling studies.

816 6.3 Hypothesis: At and below the melting level, air is dominated by detrainment of boundary
817 layer air and above the melting level in the middle free troposphere, air is more influenced by
818 entrainment and detrainment along the cloud edges. However PBL air can be ejected through the
819 anvil.

820 This hypothesis or ones like it is related to the fundamental "plumbing" of convection and what
821 fraction of air from which levels is transported where. Much of the combined Ac/aerosol
822 environment rests on the nature of convective detrainment and this detrainment phenomenon
823 may give insight into cloud dynamics and transport. The updraft core is somewhat insulated from
824 entrainment/detrainment processes, whereas parcels closer to the cloud top and edge will
825 undergo mixing with air that has originated from various levels inside and outside of the cloud.
826 Observations around clouds may reflect multiple entrainment-detrainment events (e.g., Yeo and
827 Romps, 2013). The ratio of water vapor to CO concentration in undiluted ascent should be
828 uniquely determined by the parcel's initial properties in the mixed layer, and departures from this
829 ratio within the cloud reflect the action of mixing. Detraining air from deep convection at the
830 melting level provides the strongest local source of water vapor (direct and via evaporated
831 cloud), and also the largest water vapor to CO ratio. We hypothesize that, up to the melting level,
832 detrainment is dominated by boundary layer air, whereas above this level air is more influenced
833 by entrainment and detrainment along the cloud tops and edges. It is noteworthy also that the Ac
834 cloud observed on the DC-8 was not directly at 0^{o}C, but rather 0.75^{o}C, consistent with the
835 formation of an inversion directly above it (e.g., Figure 7(b), T minimum not exactly at 0^{o}C, but
836 rather at 0.5^{o}C). These observations are in agreement with the simulations by Posselt et al.,

837 (2008) and Yasunaga et al. (2008), both of which were modeling studies that managed to form
838 melting level clouds without any predefined environmental area of stability. Perturbations in
839 temperature may be representative of large scale vertical motions on the outside of the clouds,
840 including downdrafts adjacent to regions of in-cloud upward motion. Schmidt et al., (2014)
841 suggested that the heating/cooling differentials in the vicinity of altocumulus clouds can result in
842 areas of mesoscale subsidence, further perturbing flow fields and presumably CCN intake into
843 these clouds.

844 We leave open the possibility that depending on storm dynamics, parcels in the inner core of
845 convection can be ejected into, and out of, the anvil. This overall structure, with PBL air at cloud
846 tops and bottoms, with more entrainment/detrainment dominated properties is supported in figure
847 8 where aerosol mass ratios to CO are given as well as an altitude dependence of sulfate to
848 organic matter is given. So clearly different altitude ranges have strong relationships to cloud
849 entrainment and detrainment processes and the overall convective structure. Models can certainly
850 provide insight, but considerable thought must be given to verification.

851 **7.0 Conclusions**

852 This paper presents August 12, 2013 as a case study from the SEAC^{4}RS campaign that
853 demonstrates Altocumulus cloud (Ac), aerosol and water vapor layering phenomena in a
854 convective regime over the southeastern United States (SEUS). This day was chosen due to
855 proximity of the DC-8 research aircraft to a High Spectral Resolution Lidar (HSRL) at
856 Huntsville Al. The HSRL gives period level perspective on Ac clouds and their observed aerosol
857 "halo" to help interpret in situ DC-8 data. Analysis of the meteorology of the region on this day
858 supported the assertion that aerosol was "local" to the SEUS and thus should be considered to be
859 representative of regionally forced convective environments. A 33 hour sample of lidar data was
860 presented to demonstrate the diurnal cycle of cloud and aerosol features in this convective
861 environment. The HSRL provided aerosol backscatter and precisions at or better than 5% of
862 Rayleigh, and demonstrated extraordinarily fine aerosol features in the vicinity of altocumulus
863 clouds formed in the outflow of deep convection. This day was in turn compared to a DC-8
864 profile conducted that afternoon on the downwind side of a developing storm providing in situ
865 data on the middle free troposphere aerosol environment.

866 Aside from typical boundary layer development and cirrus outflow, numerous aerosol and Ac
867 decks were identified, many of these Ac produced ice virga. Ac formed at the top of the residual
868 of the previous day's planetary boundary layer entrainment zone, where air was largely
869 influenced by boundary layer cloud detrainment. This layer formed in the morning hours, and
870 increased in base altitude with the developing boundary layer below it. Such rising may be a
871 result of mesoscale flows or cloud lofting.

872 Above the PBL-top Ac, several other combined aerosol-Ac-water vapor layers were observed.
873 Including 1) a 4 km detrainment layer that we surmise is from the very tops of cumulus
874 mediocris clouds; 2) layers at or just below 4.7 km/0^{o}C melting level representing deep
875 convective detrainment shelves, and 3) 6-7 km layers consistent with that appear to be consistent
876 with detrainment from the tops of congestus clouds. From the HSRL, Ac clouds were associated
877 with clear aerosol "halos", typically with Ac clouds on top. The intensity of aerosol backscatter
878 associated with Ac cloud halos appeared to decrease with height, beyond what would be
879 expected from adiabatic expansion. The lowest Ac clouds associated with PBL entrainment zone
880 have larger returns associated with their proximity to the polluted PBL and large accumulation
881 particle size, and hygroscopicity. However, middle free troposphere layers had markedly smaller
882 accumulation mode sizes with height, but higher CN counts. Aerosol layers above 0^{o}C had the
883 smaller accumulation model sizes and highest CN concentrations. This is consistent with further
884 cloud processing and scrubbing of detraining air at higher altitudes. Particle size and composition
885 data suggest that detraining particles undergo aqueous phase or microphysical transformations,
886 while at the same time larger particles are being scavenged.

887 Examination of profiles suggest an excess of water vapor and aerosol particles relative to CO
888 within and above the PBL entrainment zone to the melting level, and observations around clouds
889 may reflect multiple entrainment-detrainment events (e.g., Yeo and Romps, 2013). We expected
890 the ratio of water vapor to CO concentration in undiluted ascent should be uniquely determined
891 by the parcel initial properties in the mixed layer, and departures from this ratio within the cloud
892 reflect the action of mixing. Detraining air from deep convection at the melting level provides
893 the strongest local source of water vapor (direct and via evaporated cloud), and also the largest
894 water vapor to CO ratio. We hypothesize that up to the melting level, detrainment is dominated
895 by boundary layer air, whereas above this level air is more mixed involving

entrainment/detrainment along the clouds. Water vapor flux to the middle free troposphere may also be enhanced by evaporating precipitation, whereas higher altitude parcels undergo dehydration.

This work leads to numerous questions regarding relationships between aerosol layers and the properties of Ac clouds. It has been long hypothesized that increasing trends in aerosol concentrations over the past decades will result in more convective lofting, and then perhaps an indirect effect in associated Ac clouds and perhaps increases in cloud lifetimes (e.g., Parungno et al., 1994). The observation that Ac clouds have visible halos of accumulation mode particles certainly indicates that Ac are coupled with the boundary layer aerosol system. Enhancements in accumulation mode particles near Ac appear to be anti-correlated with CN for this case-likely due to available surface area for secondary mass production and or coagulation. At the same time, explosive nucleation events are visible and expected in the vicinity of clouds. All of this suggests complex CCN-Ac coupling and questions about layer flow dynamics in and around Ac and their associated aerosol layers and/or halos. Does the cycling of air through an Ac feedback into its own CCN budget? Does non-precipitating cycling enhance particle size and hence CCN number for any given supersaturation? In precipitating Ac, where are replacement CCN coming from, and do nucleating CN ever offer a supply? Or, as a hypothesis, perhaps CN events can sustain and enhance CCN populations in Ac clouds. The null hypothesis would then be that CN are consumed in individual droplets and have little overall effect in clouds with such meager updraft velocities and super saturations.

8.0 Author contributions

JR: Lead author and investigation; DP, KK, & RH: investigation and manuscript composition;
ST, CT, SW, & LZ: Flight, data, and science support; All others data providers

9.0 Acknowledgements.

We are grateful to NASA Atmospheric Composition Focus Area for their sponsorship of the SEAC^{4}RS campaign, as well as to all of the senior leadership, management and scientists that contributed to this successful mission. Funding for the deployment of the UW-HSRL was provided by the CALIPSO science team as a contribution to the SEAC^{4}RS program. Analysis of the data presented here was provided by a NASA Atmospheric Composition Campaign Data Analysis and Modeling program (NNH14AY68I) and the office of Naval Research Code 322 (N0001414AF00002). The SEACIONS network, organized at by PI Anne M. Thompson and

929 Jacquie Witte at NASA/Goddard NASA/Goddard was initially supported through a grant to
930 Pennsylvania State University (NASA NNX12AF05G). PCJ and JLJ acknowledge support from
931 NASA NNX15AT96G. We are grateful to SPEC incorporated (esp. Paul Lawson) for providing
932 cloud probe data, and Jose Jimenez (University of Colorado) for providing aerosol mass
933 spectrometer data. A portion of this research was carried out at the Jet Propulsion Laboratory,
934 California Institute of Technology, under a contract with the National Aeronautics and Space
935 Administration. Airborne data doi:10.5067/Aircraft/SEAC4RS/Aerosol-TraceGas-Cloud. All
936 SEAC^{4}RS DC-8 and geostationary data is available at https://www-
937 air.larc.nasa.gov/missions/seac4rs/. All HSRL lidar data used in this analysis is available at
938 http://lidar.ssec.wisc.edu/. MODIS satellite data used in this mission was downloaded from
939 ftp://ladsweb.nascom.nasa.gov/
940

941 **10.0 Appendix A. Supplemental meteorology analysis and imagery**

942 This appendix includes a meteorological analysis of August 12, 2013 and corresponding figures
943 to support the interpretation of this study. Included is Figure A.1 of NEXRAD reflectivity
944 spanning the study period, with higher temporal resolution when the DC-8 was sampling the
945 storm. Marked is the Huntsville site (red circle) and the location of the DC-8 aircraft. Figure A.2
946 provides GOES 13 11 μm channel images of the storm that produces Ac clouds in the Huntsville
947 lidar data in Fig. 5(d). (a) 12 Aug 2013, 1715z highlighting PBL detrained Ac clouds. Subsequent
948 panels show with an arrow the back trajectory location with corresponding cloud top
949 temperatures: A.2 (b), Initiation time for the back trajectory to the 0^{o}C cloud. (c) 10 hour back
950 trajectory endpoint to large detrainment shelf (d) Cb that formed the AC layer. Tracking his
951 observed layer suggests it was transported ~ 350 km. Figure A.3 provides images from the DC-8
952 forward video for different altitudes and layers along the DC-8 spiral.

953 To provide context to this analysis, we provide a meteorological overview of the region during
954 the early phases f the SEC4RS study. August 5-14, 2013 was a convectively active period over
955 the SEUS during the summer of 2013. Weak mid-level shortwaves or cold and stationary fronts
956 impinging on high pressure along Southern Mississippi, Alabama, and Georgia brought
957 convective activity throughout the northern SEUS and Tennessee Valley. While scattered
958 afternoon precipitation formed throughout the region, a stationary front on August 11th over
959 southern Kentucky produced more substantial cells with series of southeastward propagating
960 outflow boundaries, leading to subsequent convection over northern Alabama and Georgia
961 through the day. One such band of Cbs passed through Huntsville in the early evening on August
962 11. By August 12th, convective available potential energy (CAPE) reached >1800 J kg^{-1} at

963 sounding sites in the SEUS, leading to scattered Cbs forming in the early morning hours over
964 Tennessee and southeastern Missouri, and propagating into northern Alabama as the day
965 progressed. A significant line of convection reached the northwestern corner of Alabama, at
966 18:00 UTC (where it was sampled by the DC-8 at ~19:00 UTC), and subsequent convection that
967 formed on the eastward propagating outflow boundary reached the UAH lidar site 6 hours later.

968 Regional aerosol loadings for August 12th were consistent with air masses staying within the
969 SEUS over the past several days. AERONET AOD registered a 550 nm AOD of 0.18 at
970 Huntsville in the morning, and Terra MODIS AODs at 550 nm were reported that morning at
971 0.27 in the vicinity of the CB sampled. At the surface, regional $PM_{2.5}$ stations were reporting
972 daily averaged mass concentrations of 5-10 μg m^{-3} at CSN and SEARCH sites. Specifically at
973 Huntsville, CSN $PM_{2.5}$ ranged from 10-14 μg m^{-3} at daybreak and morning hours, dropping to 5-
974 10 μg m^{-3} in the afternoon. Global models (e.g., Session et al., 2015) suggested no significant
975 long range aerosol transport into the region aside from a pulse of African dust around August 8th
976 and 9th, three days before the case day studied here. There was no indication of smoke from the
977 Western United States impacting the area. HYSPLIT trajectories spawned at Huntsville were
978 consistent with transport via westerly winds on that day, in an air mass isolated from more
979 pollution in the north. Two day back trajectories showed that the middle troposphere air never
980 deviated from northeastern Mississippi and northwestern Alabama. Specific trajectories for Ac
981 layers identified also show origins from storms within this region over 350 km away(Fig. A.2).
982 All analyses indicate air masses near the surface through the middle troposphere were regional to
983 the SEUS over the past two days, representative of more regional pollution imbedded in a
984 regional convective regime.

985 Satellite cloud temperatures and the NEXRAD returns demonstrate the textural changes in cloud
986 fields as the day progressed from widespread cloudiness to more isolated cells. Above the mixed
987 layer, the sounding was moist but cloud free, with minor inversions at 3.4 km (perhaps indicating
988 the top of the PBL), 4.6 (0^{o}C) and 6.2 km heights. Winds were near constant at 250^{o} above the
989 mixed layer, and with steady increases to 12 m s^{-1} at the 0^{o}C melting level at 4.6 km providing
990 only a modest amount of shear (Fig 3(c)). Based on the satellite imagery and NEXRAD, the
991 fetch of the air mass over northern Alabama was over mostly Cu to a few isolated but non-
992 precipitating TCu clouds. The CAPE derived from the UAH sounding was 1650 J kg^{-1}, slightly

lower than all of the operational soundings surrounding the site at 12:00 (including Birmingham to the south at 1831 J kg^{-1} and Nashville to the north at 1811 J kg^{-1}). This neutral state in a convective regime is the midday backdrop against which investigations of clouds in the vicinity of isolated cells is performed in Section 4. By late afternoon, the region was more convectively developed, with larger but more scattered individual storms. The one observed by the DC-8 began developing at 19:00 UTC and was monitored until 20:00 UTC (the location of the DC-8 is marked on Fig A.2 (e) and (f), although the exact precipitating cell monitored was not observable by NEXRAD until 19:35 when the cloud top height grew to above 6 km)). The last NEXRAD return for this cell was at 20:00 UTC.

As the day progressed, Cbs repeatedly reformed and then propagated eastward, with one cell in a mature phase reaching UAH site at 23:00 UTC. This pattern of afternoon thunderstorms persisted for several more days, when large scale subsidence began to develop behind a weak front that passed through on August 14th.

At most levels at temperatures below -9 C intermittent ice was observed on the SPEC probes (Figure A.4) The SPEC cloud particle probes indicate ice was observed beginning about 19:27 UTC, at temperatures near -9 °C, ranging in size up to around 400-500 µm. Ice is observed on the subsequent climb to colder temperatures at 19:34 UTC (-10 °C), extending to sizes on the order of 1 mm. Intermittent ice, like that observed by the 2D-Stereo particle probe and shown in Fig A.4, is observed at subsequently colder temperatures. The 2D-S (Lawson et al. 2006) is a 2-dimensional stereo particle optical array probe that records the cross sectional image of particles from 10 µm to a few mm in size with 10 µm resolution for determining particle size, concentration, extinction, phase, and ice particle habit.

10. References

Ackerman, S. A., Toon, O. B., and Hobbs, P. V.: A model for particle microphycis, turbulent mixing, and radiative transfer in the stratocumulus-topped marine boundary layer and comparisons with measurements, J. Atmos. Sci., 1204-1236, doi:10.1174/1520-0469(1995)052<1204;AMFPMT>2.0.CO; 1995.

Alfaro-Contreras, R., Zhang, J., Reid, J. S., and S. Christopher S.,:A study of 15-year aerosol optical thickness and direct shortwave aerosol radiative effect trends using MODIS, MISR, CALIOP and CERES, *Atmos. Chem. Phys.*, 17, 13849-13868, https://doi.org/10.5194/acp-17-13849-2017, 2017.

Barrett, A. I., Hogan, R. J., and Forbes, R. M.: Why are mixed-phase altocumulus clouds poorly predicted by large-scale models? Part 1. Physical processes, *J. Geophys. Res. Atmos. Atmospheres*, 122, 9903–9926, doi: 10.1002/2016JD026321, 2017.

1072 Campbell, J. R., Vaughan, M. A., Oo, M., Holz, R. E., Lewis, J. R., and. Welton, E. J:
1073 Distinguishing cirrus cloud presence in autonomous lidar measurements, Atmos. Meas.
1074 Tech., 8, 435-449, doi: 10.5194/amt-8-435-2015, 2015.
1075 Canagaratna, M. R., Jayne, J. T., Jimenez, J. L., Allan, J. D., Alfarra, M. R., Zhang, Q.,
1076 Onasch, T. B., Drewnick, F., Coe, H., Middlebrook, A.: Chemical and microphysical
1077 characterization of ambient aerosols with the Aerodyne Aerosol Mass Spectrometer. *Mass*
1078 *Spectrom. Rev.* **2007**, *26* (2), 185–222, 2007.
1079 Canagaratna, M. R., Jimenez, J. L.,Kroll, J. H., Chen, Q.. Kessler, S. H.. Massoli, P,.
1080 Hildebrandt Ruiz, L. Fortner, E., Williams, L. R., and Wilson, K. R.: Elemental ratio
1081 measurements of organic compounds using aerosol mass spectrometry: characterization,
1082 improved calibration, and implications. *Atmos. Chem. Phys., 15* , 253–272, 2015.
1083 Clarke, A. D., Varner, J. L., Eisele, F., Mauldin, R.L., Tanner, D. and M. Litchy, M.: Particle
1084 production in the remote marine atmosphere: Cloud outflow and subsidence during ACE 1, J.
1085 Geophys. Res., 103(D13), 16397–16409, doi: 10.1029/97JD02987, 1998
1086 Cohn, S. A.: "A New Edition of the International Cloud Atlas". *WMO Bulletin*. Geneva: World
1087 Meteorological Organization. **66** (1): 2–7. ISSN 0042-9767, 2017.
1088 Corr, C. A., Ziemba, L. D., Scheuer, E., Anderson, B. E., Beyersdorf, A. J., Chen, G., Crosbie,
1089 E., Moore, R.H., Shook, M., Thornhill, K. L.,: Observational evidence for the convective
1090 transport of dust over the Central United States, J. Geophys. Res. Atmos., 121, 1306–1319,
1091 doi:10.1002/2015JD023789, 2016.
1092 DeMott, P. J., Rogers, D. C., and Kreidenweis S. M.: The susceptibility of ice formation in upper
1093 tropospheric clouds to insoluble aerosol components, J. Geophys. Res., 102(D16), 19575–
1094 19584, doi: 10.1029/97JD01138, 1997.
1095 Dunlea, E. J., DeCarlo, A. P. F., AikenA. C., Kimmel, J. R., Peltier, R. E., Weber, R.
1096 J.,Tomlinson, J., Collins, D. R., Shinozuka, Y., C. S. McNaughtonC. S.: Evolution of Asian
1097 aerosols during transpacific transport in INTEX-B. *Atmos. Chem. Phys.*, *9* , 7257–7287,
1098 2009.
1099 Eck, T. F., Holben, B. N., Reid, J. S., Arola, A., Ferrare, R. A., Hostetler, C. A.,
1100 Crumeyrolle, BS. N., Berkoff, T. A., E. J. Welton, S. Lolli, A. Lyapustin, Y. Wang, J. S.
1101 Schafer, D. M. Giles, B. E. Anderson, B. E., Thornhill, K. L., Minnis, P., Pickering, K.,
1102 Loughner, C. P., Smirnov, A., and A. Sinyuk, A. :Observations of rapid aerosol optical
1103 depth enhancements in the vicinity of polluted cumulus clouds, Atmos. Chem. Phys., 14,
1104 11633-11656, doi:10.5194/acp-14-11633-2014, 2014.
1105 Eloranta, E. W.: High Spectral Resolution Lidar Measurements of Atmospheric Extinction:
1106 Progress and Challenges," in "Aerospace Conference, 2014 IEEE," (IEEE, 2014), pp. 1–6,
1107 2014.
1108 Eloranta, E. W.: "High Spectral Resolution Lidar", in Lidar: Range-Resolved Optical Remote
1109 Sensing of the Atmosphere, K. Weitkamp editor, Springer-Verlag, New York, 2005.
1110 Fromm, M. O. Torres, O., Diner, D., Lindsey, D., Vant Hull, B., Servranck, R., Shettle, E. P.,
1111 and Li, Z.: Stratospheric impact of the Chisholm pyrocumulonimbus eruption: 1. Earth-
1112 viewing satellite perspective, J. Geophys. Res., 113, D08202, doi:10.1029/2007JD009153,
1113 2008.

1114 Garay, M. J., de Szoeke, S. P., and Moroney, C. M.: Comparison of marine stratocumulus cloud
1115 top heights in the southeastern Pacific retrieved from satellites with coincident ship-based
1116 observations, J. Geophys. Res., 113, D18204, doi:10.1029/2008JD009975, 2008.
1117 Hair, J. W., Hostetler, C. A., Cook, A. L., Harper, D. B., Ferrare, R. A., Mack, T. L., Welch,
1118 W., , L. R., and Hovis F. E., Airborne high spectral resolution lidar for profiling aerosol
1119 optical properties, Appl. Opt., 47, 6734-6752, doi: 10.1364/AO.47.006734, 2008.
1120 Heymsfield, A. J.: Microphysical structure of stratiform and cirrus clouds, In *Aerosol-Cloud-*
1121 *Climate Interaction*, ed P. V. Hobbs., Academic Press, San Diego, 97-119, 1993.
1122 Hogan, R. J., Francis, P. N., Flentje, H., Illingworth, A. J., Quante, M. and Pelon, J:
1123 Characteristics of mixed-phase clouds. I: Lidar, radar and aircraft observations from
1124 CLARE'98. Q.J.R. Meteorol. Soc., 129: 2089–2116. doi: 10.1256/rj.01.208, 2003.
1125 Holben, B.N., Eck, T. F., Slutsker, I., Tanre, D., Buis, J. P., Setzer, E. Vermote, E., Reagan, J.
1126 A., Kaufman, Y. J., Nakajima, T., Lavenu, F., Jankowiak, I., and Smirnov, A.: AERONET-
1127 a federated instrument network and data archive for aerosol characterization, Remote Sens.
1128 Environ., 66, 1-16, doi: 10.1016/S0034-4257(98)00031-5, 1998.
1129 Houze, R. A. (1993), *Cloud Dynamics*, Academic Press Inc., San Diego CA
1130 Jensen, E. J. and O. B. Toon (1992), The potential effects of volcanic aerosols on cirrus cloud
1131 microphysics, Geophys. Res. Let., 19, 1759-1762, doi: 10.1029/92GL01936
1132 Johnson, R. H., Ciesielski, P. E., and Hart, K. A., : Tropical inversions near the 0C level, J.
1133 Atmos. Sci., 53, 1838–1855, 1996.
1134 Johnson, R. H., Rickenbach, T. M., Rutledge, S. A., Ciesiekski, P. E., and Schubert W. H.,
1135 Trimodal characteristics of tropical convection, J. Clim., 12, 2397– 2418, 1999.
1136 Kaufman, Y. J. and Fraser R. S.: The effect of smoke particles on clouds and climate forcing,
1137 Science, 277, 1636-1639, 1997.
1138 Kulmala, M., Vehkamäki, H., Petäjä, T., Dal Maso, M., Lauri, A., Kerminen, V. M., Birmili,
1139 W., McMurry P. H., Formation and growth rates of ultrafine atmospheric particles: a review
1140 of observations, J. Aerosol Sci., 35, 143-176, doi: 10.1016/j.jaerosci.2003.10.003, 2004.
1141 Lawson, R. P.: Effects of ice particles shattering on the 2D-S probe. Atmos. Meas. Tech., 4,
1142 1361–1381, doi:10.5194/ amt-4-1361-2011, 2011.
1143 Lawson, R. P., Baker, B. A., Schmitt, C. G., and Jensen T. L.: An overview of microphysical
1144 properties of Arctic clouds observed in May and July during FIRE ACE. J. Geophys. Res.,
1145 106, 14 989–15 014, doi:10.1029/2000JD900789, 2001
1146 Lawson, R. P., Jensen, E., Mitchell, D. L., Baker, B., Mo, Q., and Pilson, B.: Microphysical
1147 and radiative properties of tropical clouds investigated in TC4 and NAMMA. J. Geophys.
1148 Res., 115, D00J08, doi:10.1029/2009JD013017, 2010.
1149 Lawson, R. P, O'Connor, D., Zmarzly, P., Weaver, K., Baker, B. A., Mo, Q. and Jonsson H.,
1150 The 2D-S (stereo) probe: Design and preliminary tests of a new airborne, high speed,
1151 highresolution particle imaging probe. J. Atmos. Oceanic Technol.,23, 1462–1477,
1152 doi:10.1175/JTECH1927.1, 2006.
1153 Larson, V. E., Fleishauer, R. P., Kankiewicz, J. A., Reinke, D. L., and Vonder Haar, T. H.: The
1154 death of an altocumulus cloud, Geophys. Res. Lett., 28, 2609-2612, doi:
1155 10.1029/2001GL013031, 2001.

1156 Livingston, J. M., Schmidt, B., Russell, P. B., Podolske, J. R., Redemann, J., and Diskin, G. S.:
1157 Comparison of water vapor measurements by airborne sun photometer and diode laser
1158 hygrometer on the NASA DC-8, J. Atmos. Ocean. Tech., 25, doi:
1159 10.1175/2008JTECHA1047, 2008.
1160 Loughner, C. P., Allen, D. J., Pickering, K. E., Zhang, D..-L. Shou,Y.-X., and Dickerson, R. R.:
1161 Impact of fair-weather cumulus clouds and the Chesapeake Bay breeze on pollutant transport
1162 and transformation, Atmos. Environ., 45, 4060–4072, doi:10.1016/j.atmosenv.2011.04.003.
1163 2011.
1164 Marchand, R., Ackerman, T., Smyth, M. and Rossow W. B.: A review of cloud top height and
1165 optical depth histograms from MISR, ISCCP, and MODIS, J. Geophys. Res., 115, D16206,
1166 doi:10.1029/2009JD013422, 2010.
1167 Martin, G.M., Johnson, D. W., and Spice A., The measurement and parametrization of effective
1168 radius of droplets in warm stratocumulus clouds, J. Atmos. Sci., 51, 2823-1842, doi:
1169 10.1175/1520-1469(1994)051<1823:TMAPOE>2.0.CO;2, 1994.
1170 McMillan, W. W., Evans, K. D., Barnet, C. D., Maddy, E. S., Sachse, G. W., Diskin G. S.:
1171 Validating the AIRS Version 5 CO reterival with DACOM in situ meausrements during
1172 INTEX-A and –B, IEEE Trans. On Geoscineces and Remotee Sensing, 49, 2802-2813). Doi:
1173 10.1109/TGRS.2011.2106505, 2011.
1174 Minnis, P., Nguyen, L., Palikonda, R., Heck, P. W., Spangenberg, D. A., Doelling, D. R.,
1175 Ayers, J. K., W. L. Smith, Jr., W. L., Khaiyer, M. M, Trepte, C., Avey, L. A., F.-L. Chang, F.-
1176 L., Yost, C. R., Chee, T. L., and Sun-Mack, S.: Near-real time cloud retrievals from
1177 operational and research meteorological satellites. Proc. SPIE Remote Sens. Clouds Atmos.
1178 XIII, Cardiff, Wales, UK, 15-18 September, 7107-2, 8 pp., ISBN: 9780819473387, 2008.
1179 Moser, D. H. and Lasher-Trapp S.: The Influence of Successive Thermals on entrainment and
1180 dilution in a simulated cumulus congestus, J. Atmos. Sci., 74, 375–392, doi: 10.1175/JAS-
1181 D-16-0144.1, 2017
1182 Norris, J. R.: On trends and possible artifacts in global ocean cloud cover between 1952 and
1183 1995, J. Clim., 12, 1864-1870, doi: 10.1175/1520-0442(1999)012<1864:OTAPAI>2.0.CP;2,
1184 1999.
1185 Perry, K. D. and Hobbs, P. V.: Further evidence for particle nucleation in clear air adjacent to
1186 marine cumulus clouds, J. Geophys. Res., 99, D11, 22803–22818, doi: 10.1029/94JD01926,
1187 1994.
1188 Platnick, S. and Twomey S., Determining the susceptibility of cloud albedo to changes in droplet
1189 concentration with the Advanced Very High Resolution Radiometer, J. Appl. Meteor., 33,
1190 334-347, doi: 10:1175/1520-0450(1994)033<0334:DTSOCA>2.0.CO;2, 1994.
1191 Podolske, J. R., Sachse, G. W., and Diskin G.S.:Calibration and data retrieval algorithms for the
1192 NASA Langley/Ames Diode Laser Hygrometer for the NASA Transport and Chemical
1193 Evolution Over the Pacific (TRACE-P) mission, J. Geophys. Res., 108, 8792, doi:
1194 10.1029/2002JD003156, 2003.

1195 Posselt, D. J., van den Heever S. C., and Stephens G. L.: Trimodal cloudiness and tropical stable
1196 layers in simulations of radiative convective equilibrium, Geophys. Res. Lett., 35, L08802,
1197 doi: 10.1029/2007GL033029, 2008.
1198 Pruppacher, H. R. and Klett, J. D.: Microphysics of Clouds and Precipitation, 2nd Edn., Kluwer,
1199 954 pp., 1997.
1200 Pueschel, R. F., Hallett, J., Strawa, A. W., Howard, S. D., Ferry, G. V., Foster, T., Arnott, W.
1201 P., Aerosol and cloud particles in tropical Anvil: Importance to radiation balanced, J.
1202 Aerosol. Sci., 28, 1123-1136, doi: 10.1016/S0021-8502(97)00022-0, 1997.
1203 Parungo, F., Boatman, J. F., Wilkison, S. W., Sievering, H., and Hicks, B. B.:Trends in global
1204 marine cloudiness and anthropogenic sulfur, J. Climate, 7, 434–440. doi: 10.1175/1520-
1205 0442(1994)007<0434:TIGMCA>2.0.CO;2, 1994.
1206 Radke, L. F. and P. V. Hobbs (1991), Humidity and particle fields around some small cumulus
1207 clouds, J. Atmos. Sci., 48, 1190–1193, doi:10.1175/1520-0469(1991)0482.0.CO;2. 1992.
1208 Reid J. S., Hobbs, P. V., Rangno, and A. L., Hegg D. A.: Relationships between cloud droplet
1209 effective radius, liquid water content and droplet concentration for warm clouds in Brazil
1210 embedded in biomass smoke, J. Geophys. Res., 104, 6145-6153, doi: 10.1029/1998JD200119
1211 Reid, J. S., Hyer, E., J., Johnson, R., Holben, B. N., Yokelson, R. J., Zhang, J., Campbell, J.
1212 R., Christopher, S. A., Di Girolamo, L., Giglio, L., Holz, R. E., Kearney, C., Miettinen, J.,
1213 Reid, E, A., Turk, F. J., Wang, J., Xian, P., Zhao, G., Balasubramanian, R., Chew, B. N.,
1214 Janai, S., Lagrosas, N., Lestari, P., Lin, N.-H., Mahmud, M., Nguyen, X. A., Norris, B.,
1215 Oahn, T. K., Oo, M., Salinas, S. V., Welton, E. J., and Liew S. C.: Observing and
1216 understanding the Southeast Asian aerosol system by remote sensing: An initial review and
1217 analysis for the Seven Southeast Asian Studies (7SEAS) program, Atmos. Res., 122, 403-
1218 468, doi: 10.1016/j.atmosres.2012.06.005, 2013.
1219 Reid, J. S., et al. Ground-based High Spectral Resolution Lidar observation of aerosol vertical
1220 distribution in the summertime Southeast United States, J. Geophys. Res. Atmos., 122, 2970–
1221 3004, doi:10.1002/2016JD025798, 2017.
1222 Riihimaki, L. D., McFarlane, S. A., and Comstock J. M., Climatology and formation of tropical
1223 midlevel clouds at the Darwin ARM site, J. Climate, 25, 6835–6850, doi:10.1175/JCLI-D-11-
1224 00599.1, 2012.
1225 Romps, D. M.: A direct measure of entrainment, J. Atmos. Sci., 67, 1908–1927, doi:
1226 10.1175/2010JAS3371.1, 2010.
1227 Romps, D. M., and Kuang Z.: Nature versus nurture in shallow convection, J. Atmos.
1228 Sci., 67, 1655–1666, doi: 10.1175/2009JAS3307.1, 2010.
1229 Sachse, G. W., Hill, G. F., Wade, L. O., and Perry M. G.: Fast-response, highprecision carbon
1230 monoxide sensor using a tunable diode laser absorption technique, J. Geophys. Res., vol. 92,
1231 no. D2, pp. 2071–2081, 1987.
1232 Saleeby, S. M., S. C. van den Heever, P. J. Marinescu, S. M. Kreidenweis, and P. J.
1233 DeMott (2016), Aerosol effects on the anvil characteristics of mesoscale convective
1234 systems, J. Geophys. Res. Atmos., 121, 10,880–10,901, doi: 10.1002/2016JD025082, 2016.

1235 Sassen, K.: The polarization lidar technique for cloud research: a review and current assessment,
1236 Bull. Am. Meteorol. Soc., 72, 1848–1866, 1991.
1237 Sassen, K., Liou, K. N., Kinne, S., Griffin, M.: Highly supercooled cirrus cloud water:
1238 Confirmation and climate implications, Science, 227, 411-413. 1985.
1239 Sassen, K., and Khvorostyanov V. I.: Microphysical and radiative properties of mixed-phase
1240 altocumulus: A model evaluation of glaciation effects, *Atmos. Res.*, **84**, 390–398,
1241 doi:10.1016/j.atmosres.2005.08.017, 2017.
1242 Sassen, K., and Khvorostyanov V. I., Cloud effects from boreal forest fires smoke: evidence for
1243 ice nucleation from polarization lidar data and cloud model simulations, Environ. Res. Let.,
1244 3, 025006, doi:10.1088/1748-9326/3/2/025006, 2008.
1245 Sassen, K. and Wang, Z., The clouds of the middle troposphere: Composition, radiative impact,
1246 and global distribution, Surv. Geophys., 33, 677-691, doi: 10.1007/s10712-011-9163-x, 2012.
1247 Schmidt, J., A. Ansmann, A. J. Bühl, and U. Wandinger (2015), Strong aerosol–cloud interaction
1248 in altocumulus during updraft periods: lidar observations over central Europe, Atmos. Chem.
1249 Phys., 15, 10687-10700, doi:10.5194/acp-15-10687-2015
1250 Schmidt, J. M., Flatau, P. J., and Yates R. D.: Convective cells in altocumulus observed with
1251 high-resolution radar, J. Atmos. Sci., 71, 2130-2154, doi: 10.1175/JAS-D-13-0172.1, 2014.
1252 Scott, S. G., Bui, T. P., Chan, K. R., and S. W. Bowen S. W.: The meteorological measurement
1253 system on the NASA ER-2 aircraft, J. Atmos. Ocean. Tech., 7, 525-540, 1990.
1254 Toon, O. B., et al.: Planning, implementation, and scientific goals of the Studies of Emissions
1255 and Atmospheric Composition, Clouds and Climate Coupling by Regional Surveys
1256 (SEAC^{4}RS) field mission, J. Geophys. Res. Atmos., 121, 4967–5009,
1257 doi:10.1002/2015JD024297. 2016.
1258 Twomey, S.: The Influence of Pollution on the Shortwave Albedo of Clouds, J. Atmos. Sci., 34,
1259 1149-1152., doi: 10.1175/1520-0469(1977)034<1149:TIOPOT>2.0.CO;2, 2017.
1260 Waddicor, D. A., Vaughan, G., Choularton, T. W., Bower, K. N., Coe, H., Gallagher, M.,
1261 Williams, P. I., Flynn, M., Volz-Thomas, A., Pätz, H.-W., Isaac, P., Hacker, J., Arnold, F.,
1262 Schlager, H., and Whiteway J. A.: Aerosol observations and growth rates downwind of the
1263 anvil of a deep tropical thunderstorm, Atmos. Chem. Phys., 12, 6157-6172, doi: 10.5194/acp-
1264 12-6157-2012, 2012.
1265 Wang, W., Sheng, L., Jin., H., and Han, Y.:Dust aerosol effects on cirrus and altocumulus clouds
1266 in Northwest China, J. Meteor. Res., 29, 793-805. doi: 10.1007/s13351-015-4116-9, 2015.
1267 Wang, Z., Sassen, K., Whiteman, D. N., Demoz, B. B.: Studying altocumulus with ice verga
1268 using ground based active and passive remote sensors, J. Appl. Meteor., 43, 449-460, doi:
1269 10.1175/1520-0450(2004)043<0449:SAWIVU>2.0.CO;2, 2004.
1270 Wang, G., Zhang, R., Gomez et al., M. E.: Persistent sulfate formation from London Fog to
1271 Chinese haze, *Proceedings of the National Academy of Sciences*, 113, 13630-13635, doi:
1272 10.1073/pnas.1616540113, 1998.
1273 Warren, S. G.: Global distribution of total cloud cover and cloud type amount over the ocean.
1274 NCAR Tech. Note TN-317 STR, 212 pp., 1988.

1275 Warren, S.G., Hahn, C. J., London, J., Chervin, R. M., Jenne, R.: Global distribution of total
1276 cloud cover and cloud type amount over land, NCAR Tech. Note TN-273 STR, 229 pp.,
1277 1986.
1278 Wonaschuetz, A., Sorooshian, A., Ervens, B., Chuang, P. Y., Feingold, G., Murphy, S. M.,
1279 deGouw, J., Warneke, C., and H. H. Jonsson, H. H.: Aerosol and gas re-distribution by
1280 shallow cumulus clouds: An investigation using airborne measurements, J. Geophys. Res.,
1281 117, D17202, doi: 10.1029/2012JD018089, 2012.
1347 Yang, Q., Easter, R. C., Campuzano-Jost, P., Jimenez, J. L., Fast, J. D., Ghan, S. J., Wang, H.,
1348 Berg, L. K., Barth, M. C., Liu, et al. Y., Aerosol transport and wet scavenging in deep
1349 convective clouds: A case study and model evaluation using a multiple passive tracer analysis
1350 approach, *J. Geophys. Res. Atmos.*, 120, 8448–8468, doi:10.1002/2015JD023647, 2015.
1351 Yeo, K. and Romps D. M.: Measurement of convective entrainment using Lagrangian
1352 particles, J. Atmos. Sci., 70, 266–277, doi: 10.1175/JAS-D-12-0144.1, 2013.
1353 Yasunga, K., A. Hashimoto, and M. Yoshizaki, (2008), Numerical simulations of the formation
1354 of melting-layer cloud, *Mo. Wea. Rev.*, 136, 223-241, DOI: 10.1175/2007MWR2012.1. 2008.
1355 Yasunaga, K., Yoneyama, K., Kubota, H., Okamoto, H., Shimizu, A., Kumagai, H., Katsumata,
1356 M., Sugimoto, N., Matsui I.: Melting layer cloud observed during the R/V Mirai Cruise
1357 MR01-K05. J. Atmos. Sci. 63, 3020–3032. https://doi.org/10.1175/JAS3779.1, 2006.
1358 Zhang, D., Wang, Z., and D. Liu D.: A global view of midlevel liquid-layer topped stratiform
1359 cloud distribution and phase partition from CALIPSO and CloudSat measurements, J.
1360 Geophys. Res., 115, D00H13, doi: 10.1029/2009JD012143, 2010.
1361 Zhang D., Wang, Z,. and Liu, D.: Spatial scales of altocumulus clouds observed with collocated
1362 CALIPSO and CloudSat measurements, Atmos. Res., 149, 58-69, doi:
1363 10.1016/j.atmosres.2014.05.023, 2014.
1364 Ziemba L. D., Thornhill, K. L., Ferrare, R., Barrick, J., Beyersdorf, A. J., Chen, G.,
1365 Crumeyrolle, S. N., Hair, J., Hostetler, C., Hudgins, C., Obland, M., Rogers, R., Scarino,
1366 A. J., Winstead, and E. L., Anderson, B. E.: Airborne observations of aerosol extinction by
1367 in situ and remote-sensing techniques: Evaluation of particle hygroscopicity, Geophys. Res.
1368 Lett., 40, 417–422, doi: 10.1029/2012GL054428, 2013.
1369 Zipser, E. J., Some views on hot towers after 50 years of tropical field programs and two years
1370 of TRMM data. Cloud Systems, Hurricanes, and the Tropical Rainfall Measuring Mission
1371 (TRMM): A Tribute to Dr. Joanne Simpson, Meteor. Monogr., No. 51, Amer. Meteor. Soc.,
1372 50–59, 2003.
1373
1374
1375
1376
1377

Atmos. Chem. Phys. Discuss., https://doi.org/10.5194/acp-2019-179
Manuscript under review for journal Atmos. Chem. Phys.
Discussion started: 13 March 2019

1378

Atmos. Chem. Phys. Discuss., https://doi.org/10.5194/acp-2019-179
Manuscript under review for journal Atmos. Chem. Phys.
Discussion started: 13 March 2019

Atmospheric Chemistry and Physics Discussions

Table 1. Key physical attributes (mean and± standard deviation) of detrainment layers observed from the August.12, 2017 thunderstorm. Included are altitude in mean sea level (~300 m higher than above ground level), temperature and water vapor mixing ratio (ω_v), carbon monoxide (CO), Laser Aerosol Spectrometer (LAS) number and volume at STP, 550 nm dry light scattering for particles less than 1 µm, and Aerosol Mass Spectrometer (AMS) Organic Carbon (OC) and Sulfate at STP. Layers are defined as shown in Figure 6. [&]Mixed layer properties were taken as a 5 second average just before assent. *CO instrument was in a calibration cycle for part of this layer. #Upper troposphere

	Altitude (MSL, km)	T (°C)	ω_v (g kg^{-1})	CO (ppbv)	CN>10 (cm^{-3})	LAS N (cm^{-3})	LAS CMD/mode (µm)	LAS V (µm^3 cm^{-3})	LAS VMD/mode (µm)	σ_s 550 nm (Mm^{-1})	*f*(80)	OC (µg m^{-3})	Sulfate (µg m^{-3})
ML[&]	0.94	22.1	15.5	110	2300	922	0.13/0.14	2.8	0.22/0.25	18	1.62	4.2	1.5
PBL1	1.55±0.001	18.1±0.2	13.3±0.2	93±0.6	1600±70	717±0.42	0.16/0.16	3.2±0.3	0.24/0.25	28±2.5	1.58±0.02	4.1±0.3	2.2±0.4
PBL2	2.9±0.2	10.5±1.5	9.4±0.5	76±3*	2050±2300	248±37	0.14/0.14	1.3±1.6	0.19/0.20	8±2	1.60±0.02	2.2±0.4	0.6±0.1
MT1	4.1±0.1	3.9±0.6	6.5±0.4	N/A	1532±68	112±20	N/A/<0.1	0.31±0.1	0.20/0.25	3±2	1.57±0.04	0.8±.3	0.2+/0.1
MT2	4.6±0.02	1.0±0.2	6.2±0.4	76±2	1515±720	125±36	N/A /<0.1	0.4±0.4	0.20/0.20*	3±2	1.65±0.02	0.5±0.2	0.15±0.1
MT3	6.3±0.2	-9±0.1	2.2±0.8	74±4	2893±1013	76+/12	N/A /<0.1	0.2±0.5	0.10/0.12	1±1	N/A	0.2±0.1	0.1±0.1
UT1[#]	7.8±0.2	-17.3±0.5	1.8±0.1	79±4	N/A	N/A	N/A /<0.1	N/A	N/A	N/A	N/A	0.2±0.1	0.1±0.1
UT2[#]	8.5±0.1	-21.6±0.2	0.9±0.2	80±2	8258±1192	62±10	N/A /<0.1	0.1±0.1	<0.1/0.12	1±1	N/A	0.2±0.1	0.1±0.1
UT3[#]	9.7±0.1	-30.4±0.3	0.3±0.1	76±4	7687±1980	59±12	N/A /<0.1	0.3±1.3	<0.1/0.12	1±1	N/A	1±0.3	1±0.3
UT4[#]	10.5±0.2	-38±2.3	0.4±0.1	78±1	N/A	N/A	N/A /<0.1	N/A	N/A	N/A	N/A	0.6±0.4	0.2±0.1

Atmos. Chem. Phys. Discuss., https://doi.org/10.5194/acp-2019-179
Manuscript under review for journal Atmos. Chem. Phys.
Discussion started: 13 March 2019

Atmospheric Chemistry and Physics Discussions

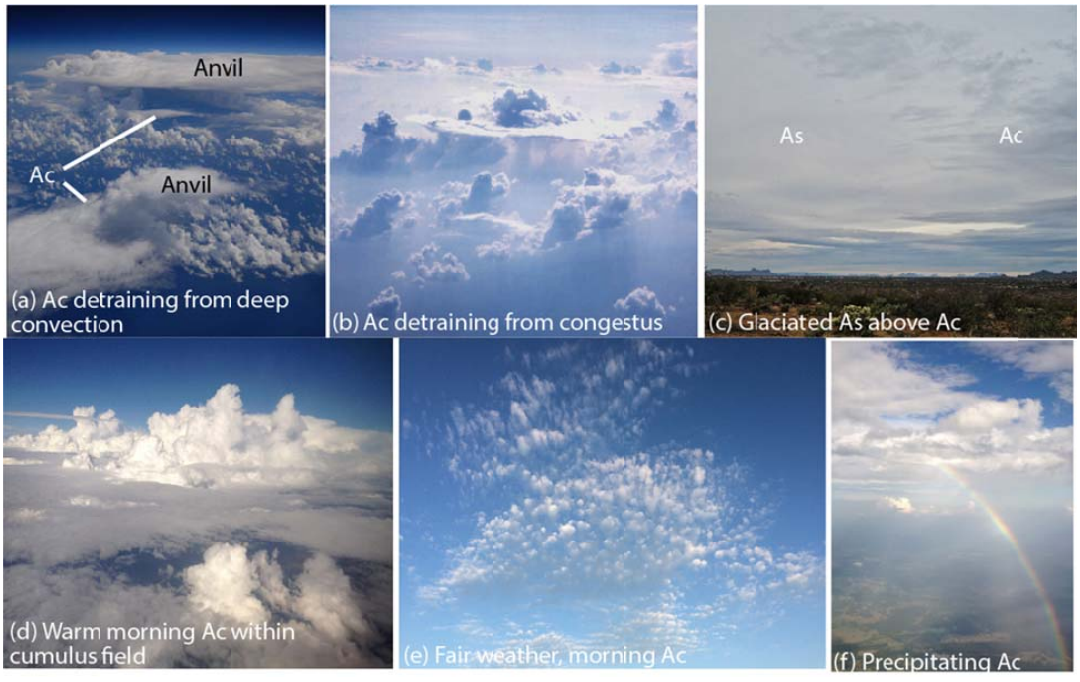

Figure 1. Cloud photographs of Ac and As characteristics. (a) Image from the NASA ER-2 showing Ac shelf clouds detraining from deep convection over the Gulf of Mexico during SEAC^{4}RS; (b) Ac detraining from cumulus congestus in a field of biomass burning smoke over Brazil (Reid et al., 1999); (c) mixed field of As above Ac clouds during a convectively active period in Arizona ; (d) Warm Ac clouds over developing cumulus field over west Texas during SEAC^{4}RS ; (e) Morning fair weather Ac field over Monterey CA; (f) precipitating thin Ac clouds over central Texas during SEAC^{4}RS (Photo credit, (a) S. Broce, NASA; (b) & (c) A. Rangno, enhanced for contrast; (d) - (f), J. S. Reid).

Atmos. Chem. Phys. Discuss., https://doi.org/10.5194/acp-2019-179
Manuscript under review for journal Atmos. Chem. Phys.
Discussion started: 13 March 2019

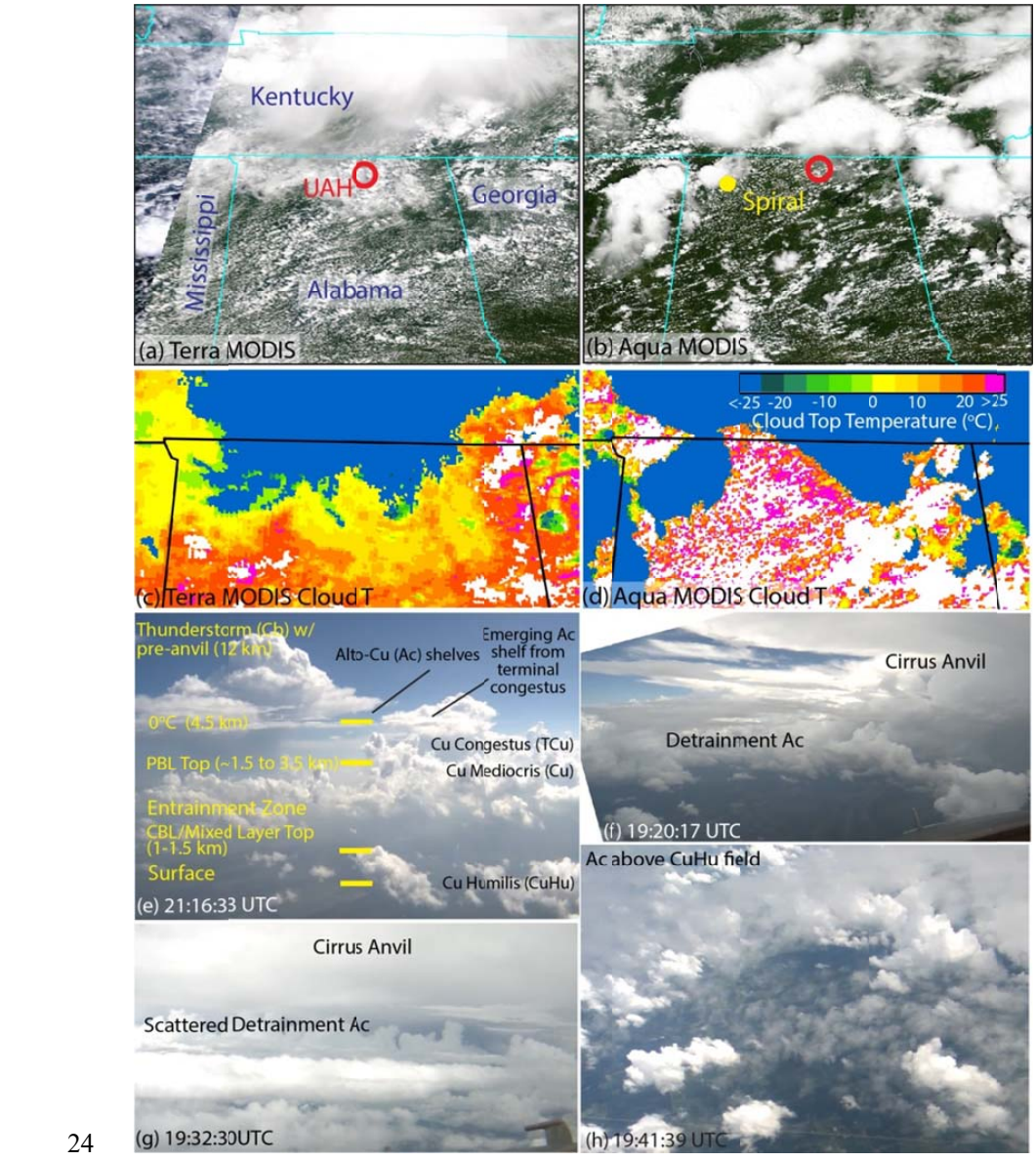

Figure 2. MODIS (a) Terra (16:00 UTC) and (b) Aqua (19:14 UTC) images, with markers indicating the location of the UAH lidar site (red) and DC-8 spiral (yellow) for August 12, 2013. Corresponding MYD06 cloud top temperatures zoomed onto northern Alabama are provided in (c) and (d). Also included are annotated camera images from the NASA DC-8 demonstrating cloud types (e) image just after profile components end; (f) forward images as the DC8 was about to enter a detrainment Ac at 4.4 km (g) forward image of the DC-8 while sampling 6.5 km aerosol layer; (h) nadir images of an Ac detrainment shelf exiting a Cb over a field of Cu.

Atmos. Chem. Phys. Discuss., https://doi.org/10.5194/acp-2019-179
Manuscript under review for journal Atmos. Chem. Phys.
Discussion started: 13 March 2019

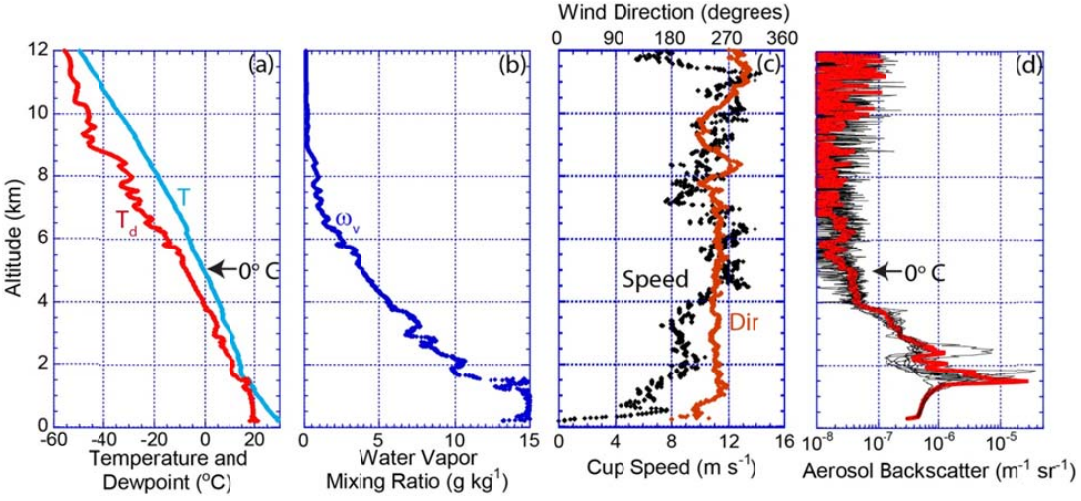

Figure 3. SEACIONS radiosonde release on August 12th, 2013 18:40 Z/13:40 CDT at Huntsville (Altitude in MSL, 200 m greater than ground level). (a) Temperature and dewpoint; (b) water vapor mixing ratio; (c) wind cup speed and direction. (d) 5 minute aerosol backscatter profiles from the UW-HSRL at Huntsville for the two hours after the radiosonde release, with the mean value in red.

Atmos. Chem. Phys. Discuss., https://doi.org/10.5194/acp-2019-179
Manuscript under review for journal Atmos. Chem. Phys.
Discussion started: 13 March 2019

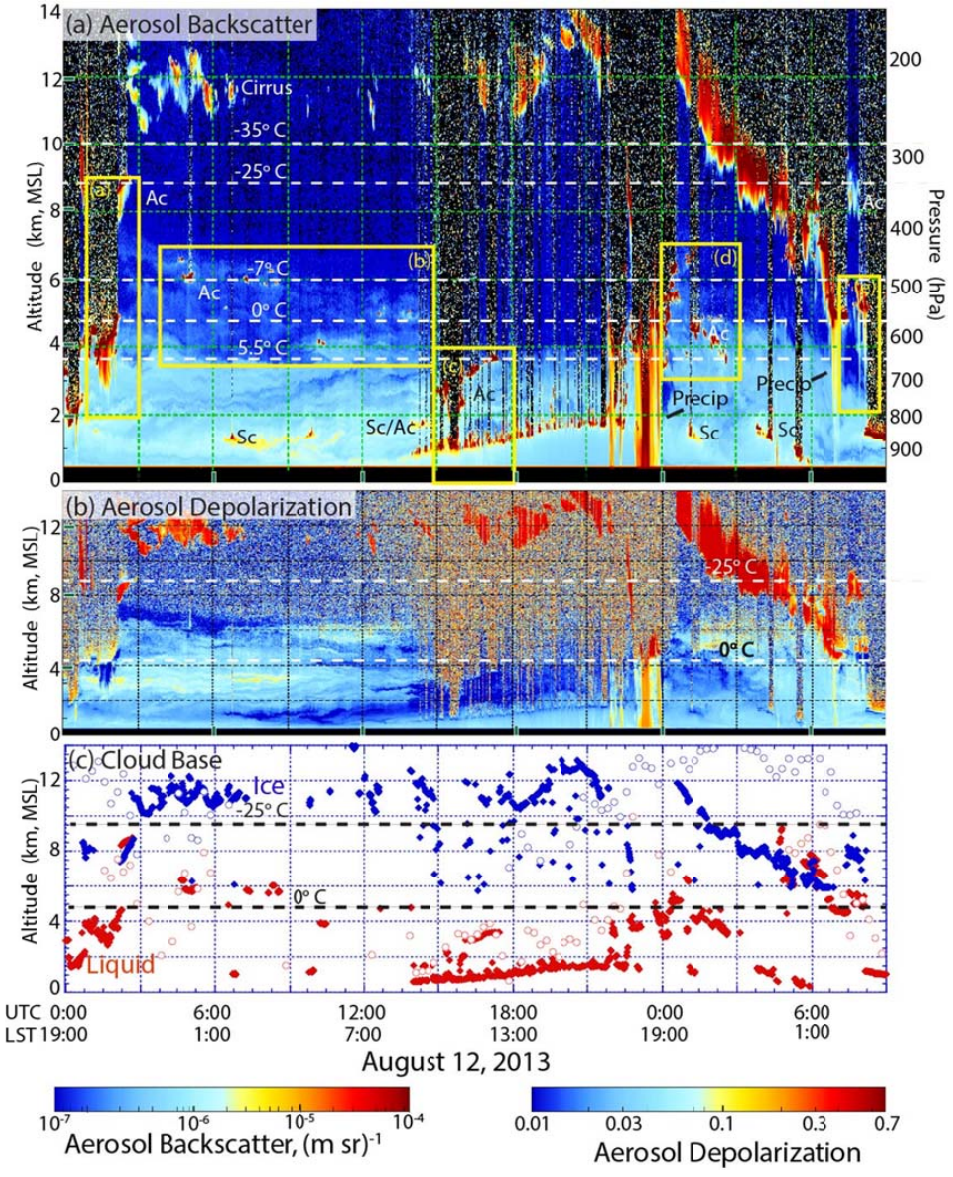

Figure 4. Example lidar data for August 12, 2013. UW HSRL aerosol (a) backscatter and (b) depolarization from the surface to 14 km AGL. Listed are cloud types, phenomenon and, from a 13:30 radiosonde release, key temperature isopleths. Also shown in (c) are liquid and ice cloud bases (solid) from the ground based HSRL, and liquid and cloud tops from GOES-13 (open). To convert from AGL to MSL, subtract 220 m.

Atmos. Chem. Phys. Discuss., https://doi.org/10.5194/acp-2019-179
Manuscript under review for journal Atmos. Chem. Phys.
Discussion started: 13 March 2019

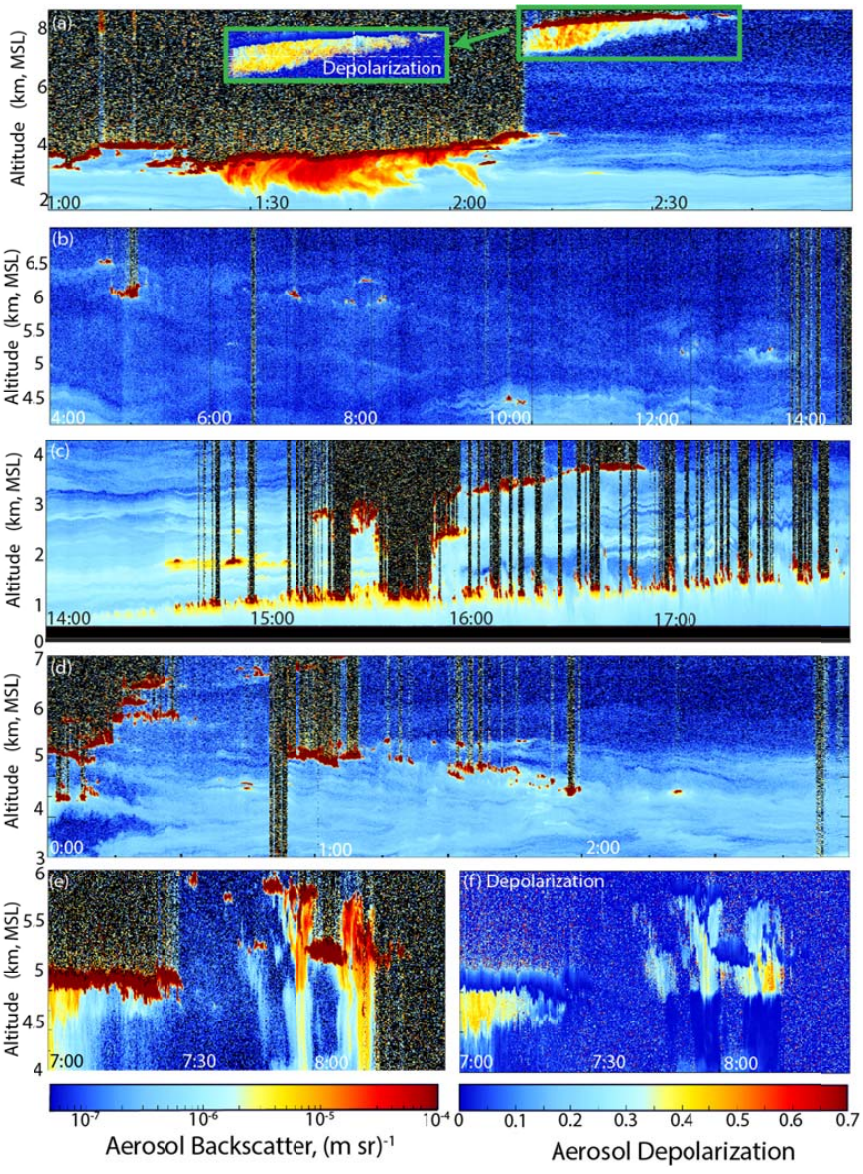

Figure 5. Aerosol backscatter for inset boxes as labeled in Figure 4 of key altocumulus and aerosol features for the August 12, 2013 case. Included is aerosol depolarization where ice is prevalent including an inset in (a), and a depolarization in (f) corresponding to (e). All times are UTC.

Atmos. Chem. Phys. Discuss., https://doi.org/10.5194/acp-2019-179
Manuscript under review for journal Atmos. Chem. Phys.
Discussion started: 13 March 2019

Atmospheric Chemistry and Physics Discussions

56

57

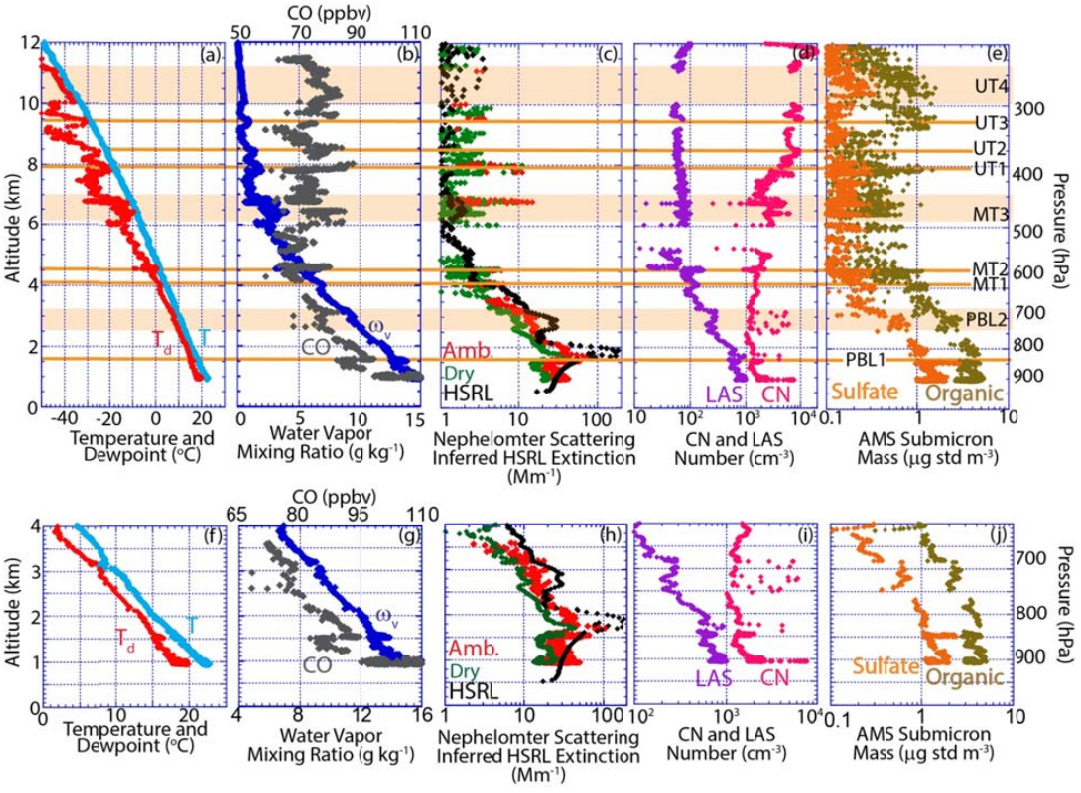

58

59 Figure 6. DC-8 aircraft spiral sounding data initiated at August 12, 2013 19:10:30 UTC on the
60 downwind side of a thunderstorm over northwest Alabama. Altitudes are relative to mean sea
61 level, ~ 300 m higher than AGL. Included is (a) Temperature and dew point; (b) Water vapor
62 mixing ratio (ω_v) and CO; (c) DC-8 total ambient and fine dry 550 nm nephelometer with the
63 ground based UW HSRL derived extinction (lidar ratio=55 sr^{-1}) at Huntsville Al; (c) Number
64 concentration from laser aerosol spectrometer (LAS, d_p>0.1 µm) and condensation nuclei (CN,
65 dp>10 nm); (e) Aerosol mass spectrometer organic materials and sulfate. Key moisture and
66 aerosol layers as discussed in the text are marked as orange lines or bands.(f)-(j), same as (a)-(e)
67 expanded in the vertical to enhance PBL feature readability and the legends are equivalent.

68

69

Atmos. Chem. Phys. Discuss., https://doi.org/10.5194/acp-2019-179
Manuscript under review for journal Atmos. Chem. Phys.
Discussion started: 13 March 2019

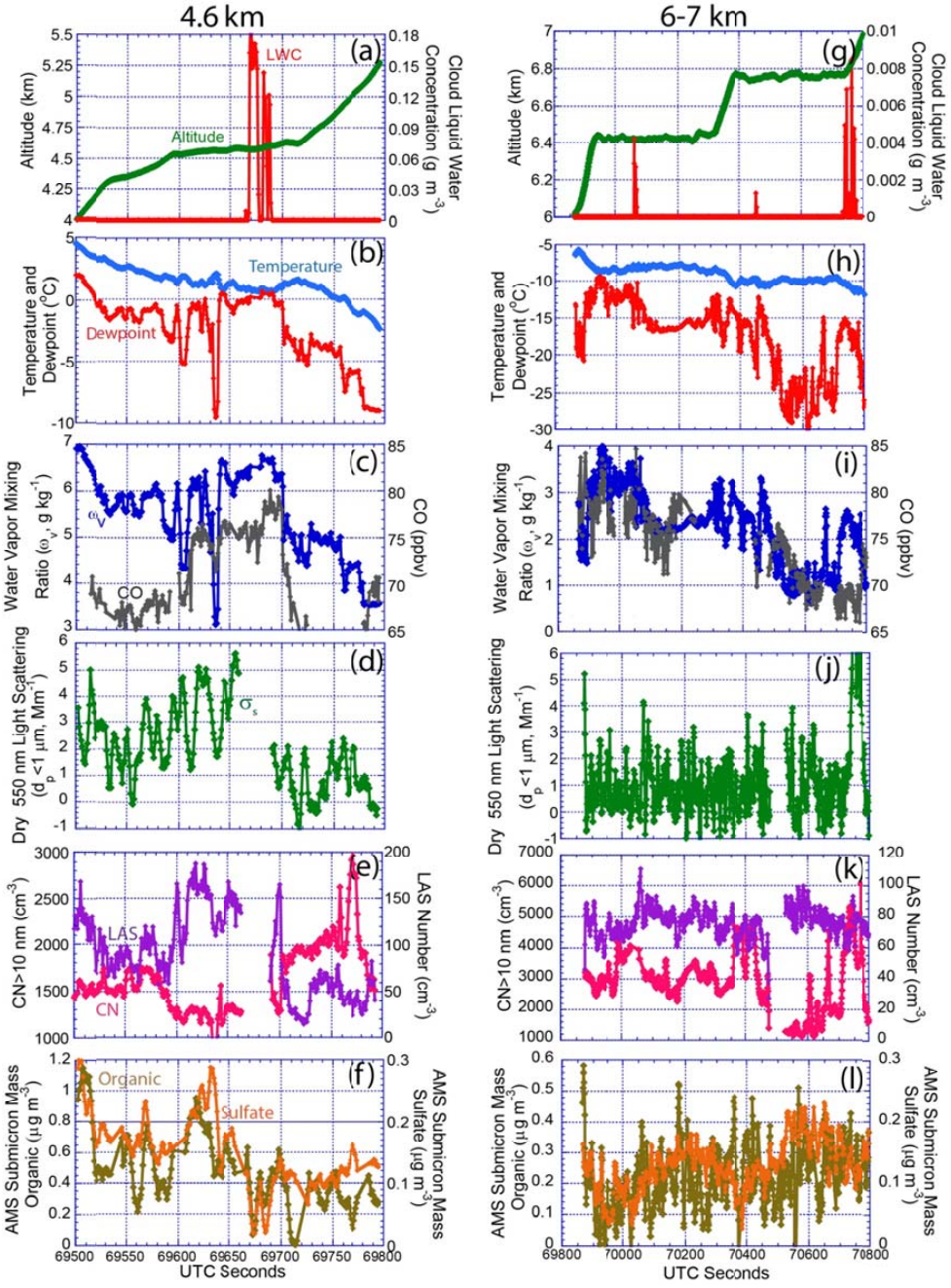

Figure 7. Time series of key meteorology, cloud and aerosol properties entering a detrainment shelf cloud on Aug 12, 2014. The legends for the graphs on the left are the same for graphs on the right

Atmos. Chem. Phys. Discuss., https://doi.org/10.5194/acp-2019-179
Manuscript under review for journal Atmos. Chem. Phys.
Discussion started: 13 March 2019

Atmospheric Chemistry and Physics Discussions

74

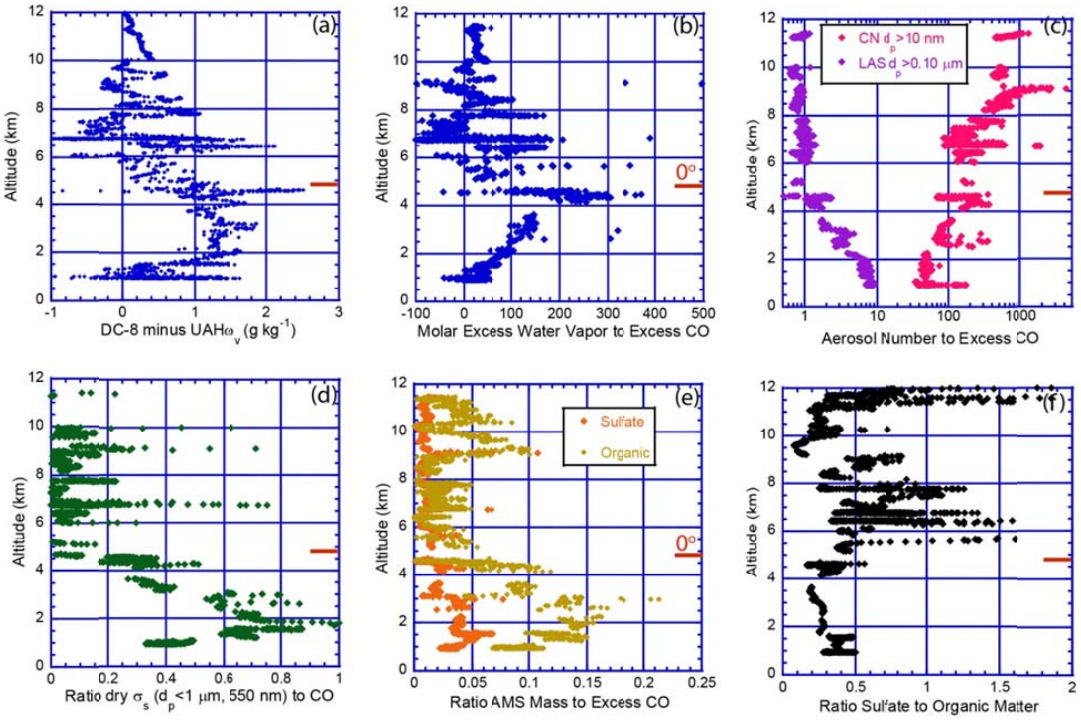

75

76

77 Figure 8. (a) Difference in water vapor mixing ratio between the DC-8 profile and the
78 SEACONS radiosonde release at Huntsville. Profiles of key constituents relative to excess CO
79 including (b) excess water vapor to excess CO; and (c) aerosol number; (d) dry light scattering;
80 (e) organic carbon and sulfate to excess CO; (f) ratio of sulfate to particulate organic matter.

81

Atmos. Chem. Phys. Discuss., https://doi.org/10.5194/acp-2019-179
Manuscript under review for journal Atmos. Chem. Phys.
Discussion started: 13 March 2019

Atmospheric Chemistry and Physics Discussions

82

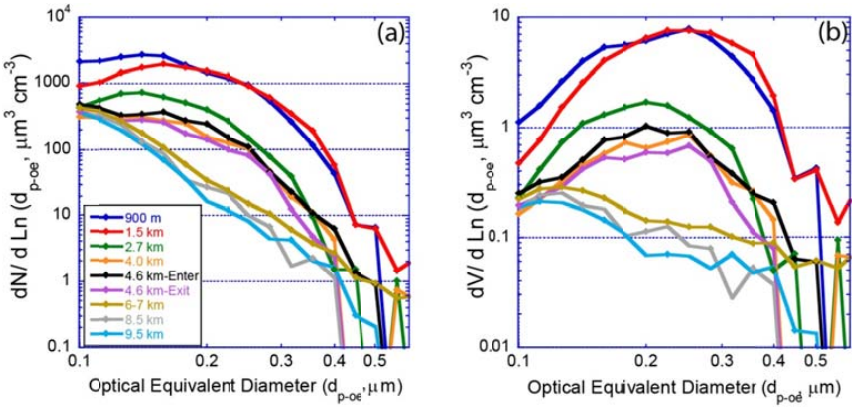

83

84 Figure 9. Laser Aerosol Spectrometer-LAS (a) number and (b) volume distributions of aerosol
85 layers as a function of altitude. The legends for the two graphs are the same.

86

Atmos. Chem. Phys. Discuss., https://doi.org/10.5194/acp-2019-179
Manuscript under review for journal Atmos. Chem. Phys.
Discussion started: 13 March 2019

Atmospheric Chemistry and Physics Discussions

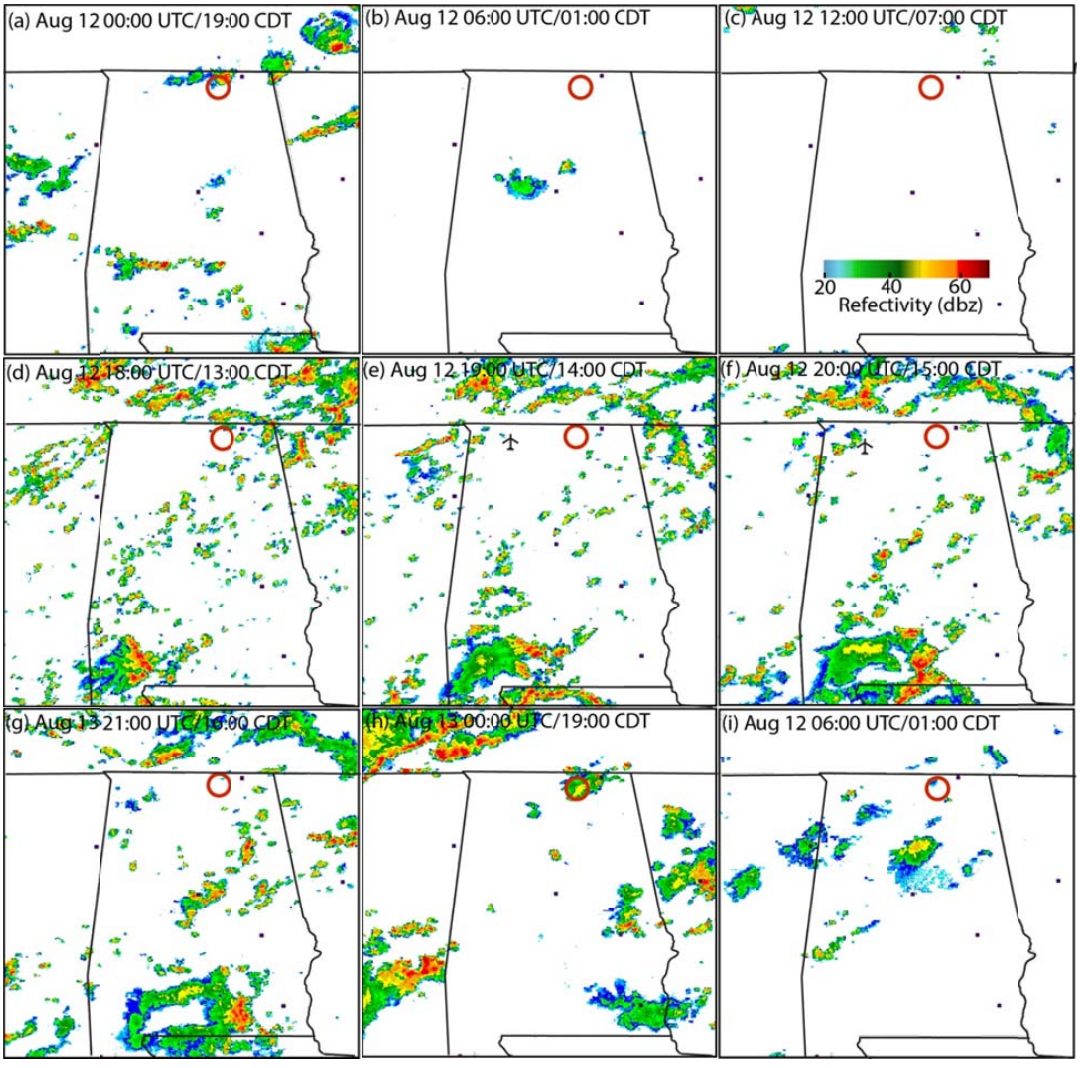

Figure A.1. NEXRAD radar reflectivity composites for August 12, 2013 study case. The red circle indicates…… Pull the color bar outside so it is obvious that it can be used for all the graphs???

Atmos. Chem. Phys. Discuss., https://doi.org/10.5194/acp-2019-179
Manuscript under review for journal Atmos. Chem. Phys.
Discussion started: 13 March 2019

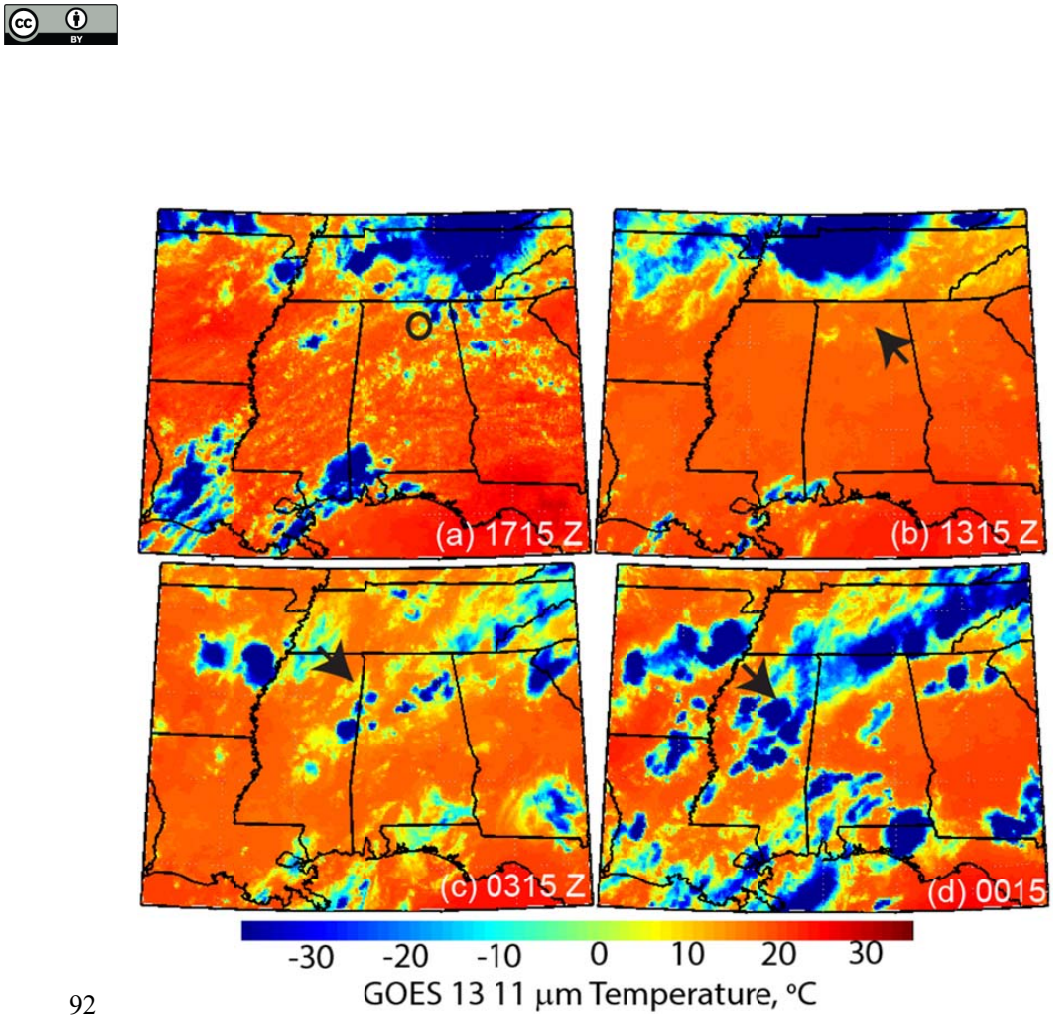

Figure A.2. GOES 13 11 μm channel images of the storm leading to AC clouds in the Huntsville lidar data in Figure 5. (a) 12 Aug 2013, 1715z of PBL detrained AC clouds. (b) Initiation of back trajectory for 0°C cloud. (c) 10 hrs back trajectory endpoint to large detrainment shelf (d) Cb that formed the AC layer.

Atmos. Chem. Phys. Discuss., https://doi.org/10.5194/acp-2019-179
Manuscript under review for journal Atmos. Chem. Phys.
Discussion started: 13 March 2019

Figure A.3. Forward camera mages from the DC-8 forward video taken from the leeward spiral along the sampled thunderstorm on August 12, 2014 over northwestern Alabama

Atmos. Chem. Phys. Discuss., https://doi.org/10.5194/acp-2019-179
Manuscript under review for journal Atmos. Chem. Phys.
Discussion started: 13 March 2019

Atmospheric Chemistry and Physics Discussions

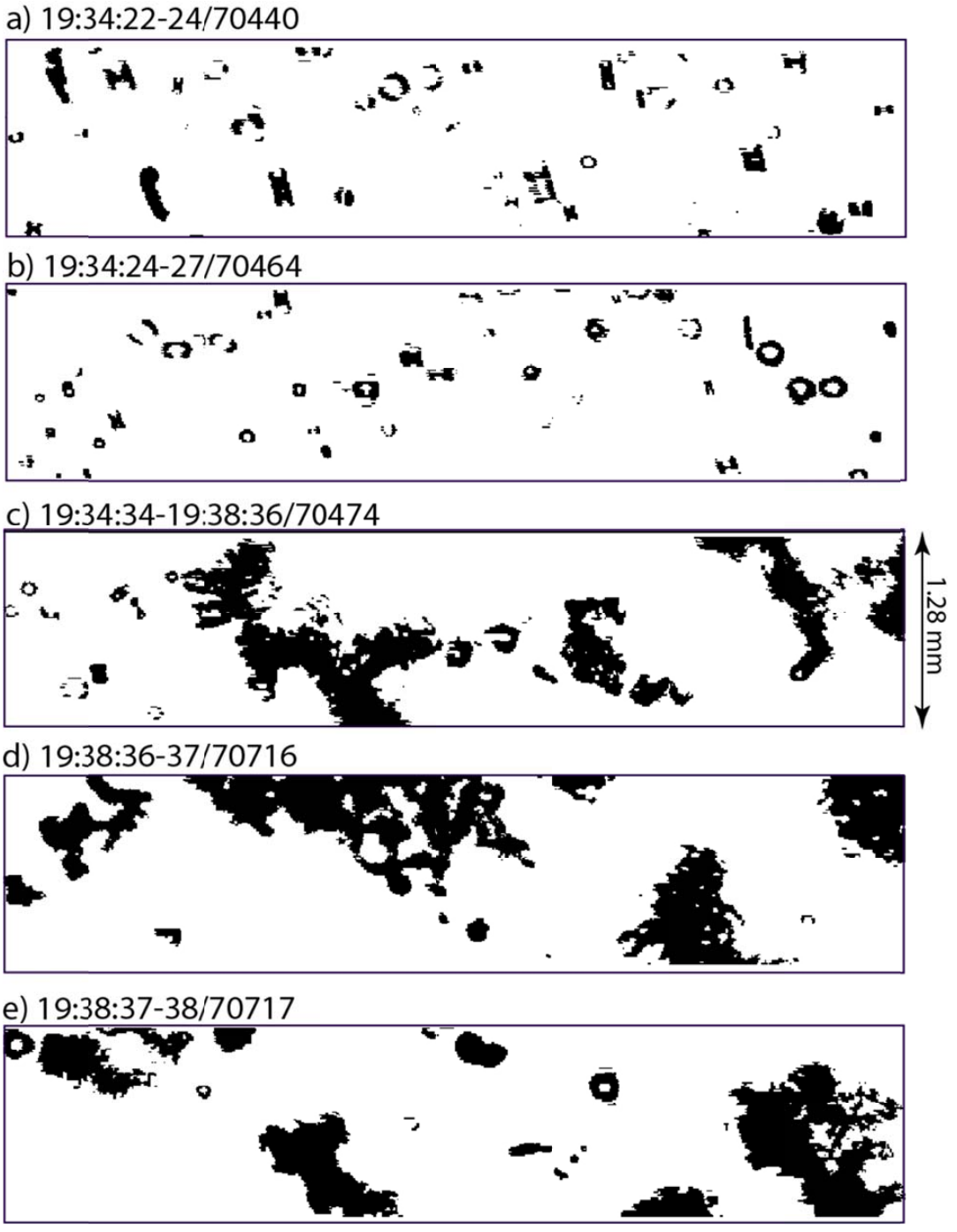

105

Atmos. Chem. Phys. Discuss., https://doi.org/10.5194/acp-2019-179
Manuscript under review for journal Atmos. Chem. Phys.
Discussion started: 13 March 2019

Atmospheric Chemistry and Physics Discussions

106 Figure A.4. 2D-S images of ice for selected periods during layer sampling associated with the
107 right column of Fig. 7.. Temperatures were -~-10°C, at an altitude of 6.75 km. Annulus are ice
108 imaged out of focus.